Journal of Energy Storage 44 (2021) 103324

Contents lists available at ScienceDirect

Journal of Energy Storage

journal homepage: www.elsevier.com/locate/est

Lithium-ion battery cathode and anode potential observer based on reduced-order electrochemical single particle model

Liuying Li [a,c], Yaxing Ren [a,c,*], Kieran O'Regan [b,c], Upender Rao Koleti [a], Emma Kendrick [b,c], W. Dhammika Widanage [a,c], James Marco [a,c]

[a] WMG, University of Warwick, Coventry, CV4 7AL, UK
[b] School of Metallurgy and Materials, University of Birmingham, Birmingham, B15 2TT, UK
[c] The Faraday Institution, Harwell Campus, Didcot, OX11 0RA, United Kingdom

ARTICLE INFO

Keywords:
Lithium-ion battery
Electrochemical model
Model order reduction
Cathode and anode potential estimation
Luenberger observer

ABSTRACT

The fast charging of Lithium-ion batteries within electric vehicles can accelerate the side reaction of lithium plating due to an anode potential that occurs as state of charge increases. It is important to monitor the anode potential during battery charging, but it is not practical to measure the inside of the battery directly for a commercial cell. This paper proposes an observer for estimating the cathode and anode potentials based on the reduced-order electrochemical model, which only needs terminal voltage to track the cathode and anode potentials and their internal charge concentration. The observer design is based on the model order reduction and linearisation of a single particle model with electrolyte (SPMe) to achieve acceptable accuracy with a low calculation cost. The linearised model and the designed observer are validated by the experimental results of a three-electrode cell. The results show that the linearised model reduces the operation time by more than 99% compared with the full-order SPMe model using the same processor. The results also verify that the root mean square error of the cathode and anode potential estimated by the observer is less than 0.02 V for a charging current range from 0.3C to 1C. This shows that the developed cathode and anode potential observer based on the reduced-order electrochemical model can be used within real-time control applications to detect the anode potential in real time to avoid battery degradation caused by lithium plating.

1. Introduction

As one of the most important energy storage systems, lithium-ion batteries play an increasingly important role in the smart grid and electrified vehicle applications [1]. However, the lithium-ion battery still poses many challenges in its application to electric vehicles (EV). One amongst them is to improve charging speed without accelerating degradation within the battery [2, 3]. One of the most severe degradation issues during fast charging is the occurrence of lithium plating in the Li-ion batteries using graphite as anode material [3, 4]. For graphite, the most commonly used anode electrode material, the formation of metallic Li on the graphite anode can occur during fast charging when the anode potential drops below the lithium reference potential [5]. Lithium plating results in the loss of cyclable lithium reduces the available energy capacity in a battery. Furthermore, lithium plating can compromise the battery safety if dendrites are formed out of the metallic depositions. These dendrites may result in an internal short circuit if they grow through the separator towards the cathode [6]. Therefore, advanced battery management systems (BMSs) should detect and prevent lithium plating to ensure safe operation of lithium-ion batteries. The observation of anode potential to avoid potentials below the reference decreases the occurrence of Li plating and thus to reduces its negative impact with high charging rate.

Experimental approaches can be found from literature to measure and control anode potential [7–10]. A reconstructed three-electrode cell with the support of harvested electrodes from a commercial cell is suggested to monitor the anode potential and to identify a charging

Abbreviations: EV, Electric vehicle; BMS, Battery management system; P2D, Pseudo two dimensional; SPMe, Single particle model with electrolyte; ECM, Equivalent circuit model; FOM, Full order model; ROM, Reduced order model; LM, Linearised model; OCP, Open circuit potential; SOC, State of charge; CC, Constant current; CV, Constant voltage; PDE, Partial differential equation; ODE, Ordinary differential equation; FDM, Finite difference method; RG, Residue grouping; RMSE, Root mean square error; NEDC, New European drive-cycle.

* Corresponding author.
E-mail address: yaxing.ren@warwick.ac.uk (Y. Ren).

https://doi.org/10.1016/j.est.2021.103324
Received 17 June 2021; Received in revised form 24 September 2021; Accepted 26 September 2021

Nomenclature

$c_s^{\pm}$	Lithium concentration in solid phase mol/m^3
c_e^j	Lithium concentration in electrolyte phase mol/m^3
$c_{ss}^{\pm}$	Lithium concentration in solid phase at particle surface mol/m^3
$\phi_s^{\pm}$	Solid electric potential V
$\phi_e^{\pm,s}$	Electrolyte electric potential V
$U^{\pm}$	Open circuit potential V
$\eta^{\pm}$	Over-potential V
$i_e^{\pm}$	Ionic current A/m^2
$j_n^{\pm}$	Molar ion flux mol/m^{2-}s
$i_0^{\pm}$	Exchange current density A/m^2
I	Applied current A
V_t	Terminal voltage V

profile [6]. However, transferability of the results obtained from the reconstructed cell to the corresponding commercial cell is difficult because of the extraction procedure that can modify the electrodes physically and chemically and use a different cell construction and electrolyte compared to the commercial cell [11]. Alternatively, insertion of a reference electrode into a commercial cells is proposed to measure the anode potential directly [12]. However, the material used for the reference electrode and its stability over many cycles and the insertion procedure can alter the battery operation. Therefore, measurement of the anode potential with these approaches may not optimise the charging performance.

As an alternative to the experimental approaches, several studies have been conducted to estimate the anode potential using models of Li-ion cells. The models of Li-ion cells can be mainly divided into equivalent circuit model (ECM), data driven model and electrochemical model [13]. The ECM is simple and widely used for BMS design [14], consistency evaluation [15] and battery thermal prediction [16, 17]. In addition, Koleti et al. developed the real-time impedance tracking method by measuring different parameters during charging to detect the lithium plating [18, 19]. However, the ECM is imprecise to model interior electrochemical properties [20] and has limited capability to predict battery degradation. Lin proposed a data-driven approach that uses the long short-term memory neural network to predict the anode potential [21]. However, the approach is based on data instead of physically informed model. The accuracy will depend on the data chosen to train and the operation condition may be limited. Alternatively, White et al. developed a physics based mathematical model to study lithium deposition on the anode electrode under a variety of operating conditions such as different ambient temperatures and charge C-rates [22]. The model is too computationally expensive including deep understanding of battery chemistry and difficult to implement in real time control tasks. Therefore, the electrochemical model is widely developed to model the physical behaviour of Li-ion battery cells.

Some recent research proposed advanced health-aware state estimation methods based on high dimensional electrochemical models [23, 24]. The most commonly used electrochemical model is the Doyle-Fuller-Newman model, alternatively called the pseudo-two-dimensional (P2D) model [25–28]. The traditional P2D model can accurately model the physical behaviour of internal dynamics inside the cell [29]. A recent study use P2D models for online anode potential estimation [30]. However, the P2D model is very complicated because it involves a coupled system of differential algebraic equations (DAE). Therefore, it is difficult to be implemented for applications where computational speed is critical, such as real-time optimisation and control [31]. Some spatial semidiscretisation approaches have been developed to solve the P2D model, including finite differences method [32, 33], finite element method [34] and finite volume method [35]. In recent literatures, there is a trend to combine the ECM and electrochemical model to obtain the advantages of both, i.e. high computational speed and physically meaningful [36]. A recent study proposed a computationally efficient state estimation method for Li-ion batteries based on a P2D model with thermal dynamics to improve accuracy, calculation speed and robustness [37]. On the other hand, simpler electrochemical models began to attract the attention of many researchers. One of the simpler models is the single particle model with electrolyte (SPMe) [38], which uses the assumption of a single particle to model the average behaviour of each solid phase for the anode and cathode. The SPM, as discussed in a number of academic papers [39–42], is simpler to solve than the P2D model but involves several coupled partial differential equations (PDEs), which are computationally intractable for real-time implementation. Thus, it is necessary to design an observer based on the electrochemical model of Li-ion cells for real-time optimisation and control applications.

In order to find a simple and effective method to obtain the anode potential with acceptable accuracy and low cost, this paper proposes an observer method, which simplify the SPMe model with order reduction and linearisation to achieve higher calculation efficiency. The main novelty of this article lies in the model reduction and linearisation of the electrochemical model of Li-ion batteries, and the observer design for predicting the potential of the cathode and anode. The designed observer greatly reduces the model calculation time under the premise of ensuring the accuracy in states estimation in a real-time application. The developed cathode and anode potential observers are verified by experimental results, including CC—CV charging, CC discharging and real-world driving cycles, using a three-electrode battery.

The rest of this paper is organised as follows. Section 2 derives the SPMe model, the model's numerical solution and the model order reduction technique applied to reduce the order of the model. In Section 3, the reduced order model is linearised at different operating points and the Luenberger observer is designed based on the linear reduce order model. Section 4 presents the model parameterisation and validation process using experimental data. Section 5 investigates the observer performance of tracking the states of a battery model in simulation and a three-electrode cell during experimental validation, respectively. Finally, conclusions and future work are drawn in Section 6.

2. Electrochemical model and order reduction methods

The Pseudo-two-Dimensional (P2D) model and the Single Particle Model with electrolyte (SPMe) are the most popular electrochemical-based models [43]. The P2D model is very complicated because it involves a coupled system of differential algebraic equations (DAE) and it makes the P2D model difficult to be implemented for real-time optimisation and control [31]. The SPMe model is a simplification of P2D model by using a single particle to model the average behaviour of each solid phase for anode and cathode [38]. The process of the model development for observer design from original SPMe model is shown in the flowchart in Fig. 1.

The original SPMe model contains several coupled partial differential equations (PDEs) that are computationally intractable for real-time implementation. Different numerical methods can be applied on the diffusion PDEs of SPMe model, such as finite difference method and finite element method [44, 45]. But these methods will generate a very high order model, which is defined as full-order model (FOM) in this paper. The FOM greatly increases the amount of computation of the model, making it not suitable for real-time control that requires high computing speed. Therefore, model order reduction techniques can be used to reduce the model order while maintaining the desired level of accuracy [46, 47]. There are many method can be used for model order reduction, such as the residue grouping [48] and balance truncation methods [49]. With the reduced order model (ROM), the number of states is greatly reduced for less computational load. However, the

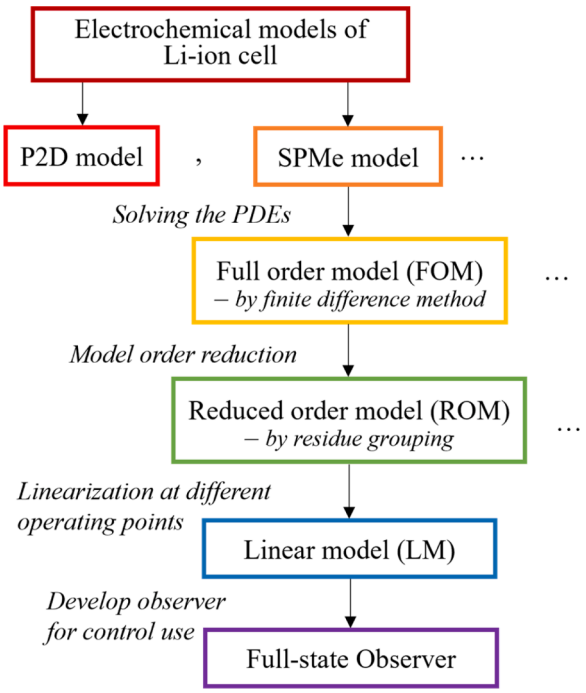

Fig. 1. Flowchart of model simplification and observer development.

resulting ROM is typically nonlinear model that contains many nonlinear operators in the relationship between lithium concentration and open circuit potential, over-potential and electrolyte potential. In order to further reduce the computing time while maintaining its accuracy, the linearisation techniques are used to linearise the ROM model. Here, the Luenberger observer is designed based on the linearised model (LM) to estimate the full states of the ROM model. The detailed process of model order reduction of the SPMe model is given in the following sections. The following sections describe the observer design process step by step.

2.1. Single particle model with electrolyte

The SPMe model derived by Scott J. Moura is a simplification of the Newman model [50]. A detailed description of this model has been presented in [43] and will therefore not be repeated here. The positive and negative electrodes are modelled with spherical particles surrounded by the electrolyte. The Li-ion intercalation and de-intercalation processes are performed through the surface area of these particles [43]. The SPMe is derived under several assumptions [38]. These assumptions ultimately render a model consisting of two diffusion PDEs for electrode concentrations, one combined diffusion PDE for electrolyte concentrations, and a nonlinear output function relating to the surface concentration of the solid, the boundary concentration of the electrolyte, and the current, as shown in Fig. 2.

The governing equations of the solid-state diffusion are [38]:

$$\frac{\partial c_s^+}{\partial t}(r,t) = \frac{1}{r^2}\frac{\partial}{\partial r}\left[D_s^+ r^2 \frac{\partial c_s^+}{\partial r}(r,t)\right] \tag{1}$$

$$\frac{\partial c_s^-}{\partial t}(r,t) = \frac{1}{r^2}\frac{\partial}{\partial r}\left[D_s^- r^2 \frac{\partial c_s^-}{\partial r}(r,t)\right] \tag{2}$$

The boundary conditions are:

$$\frac{\partial c_s^\pm}{\partial t}(0,t) = 0 \tag{3}$$

$$\frac{\partial c_s^\pm}{\partial t}(R_s^\pm,t) = \pm\frac{1}{D_s^\pm F a^\pm L^\pm} I(t) \tag{4}$$

The governing equations of the electrolyte diffusion are [38]:

$$\frac{\partial c_e^+}{\partial t}(x,t) = \frac{\partial}{\partial x}\left[\frac{D_e^+}{\varepsilon_e^+}\frac{\partial c_e^+}{\partial x}(x,t)\right] - \frac{(1-t_c^0)}{\varepsilon_e^+ F L^+} I(t) \tag{5}$$

$$\frac{\partial c_e^{sep}}{\partial t}(x,t) = \frac{\partial}{\partial x}\left[\frac{D_e^{sep}}{\varepsilon_e^{sep}}\frac{\partial c_e^{sep}}{\partial x}(x,t)\right] \tag{6}$$

$$\frac{\partial c_e^-}{\partial t}(x,t) = \frac{\partial}{\partial x}\left[\frac{D_e^-}{\varepsilon_e^-}\frac{\partial c_e^-}{\partial x}(x,t)\right] + \frac{(1-t_c^0)}{\varepsilon_e^- F L^-} I(t) \tag{7}$$

The boundary conditions are [38]:

$$\frac{\partial c_e^\pm}{\partial t}(0^\pm,t) = 0 \tag{8}$$

$$D_e^- \frac{\partial c_e^-}{\partial x}(L^-,t) = D_e^{sep}\frac{\partial c_e^{sep}}{\partial x}(0^{sep},t) \tag{9}$$

$$D_e^{sep}\frac{\partial c_e^{sep}}{\partial x}(L^{sep},t) = D_e^+ \frac{\partial c_e^+}{\partial x}(L^+,t) \tag{10}$$

The governing equation for the over potential is [38]:

$$j_n^\pm(t) = \frac{1}{F} i_0^\pm(t)\left[e^{\frac{\alpha_a F}{RT}\eta^\pm(t)} - e^{-\frac{\alpha_c F}{RT}\eta^\pm(t)}\right] \tag{11}$$

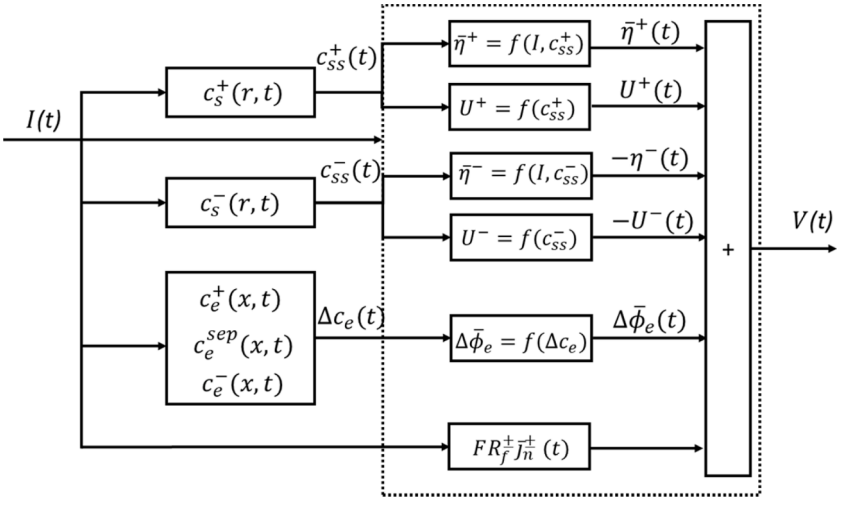

Fig. 2. Block diagram of SPMe.

The meaning of each term employed in model formulation and their respective measurements units are defined in [38]. As the SPMe model simplifies the solid phase Li concentration in each electrode, the concentration is constant in spatial coordinate x and uniformly distributed in time. Mathematically, the molar ion flux can be derived as proportional to current [38]:

$$j_n^{\pm}(t) = \mp\frac{I(t)}{Fa^{\pm}L^{\pm}} \tag{12}$$

Based on [50], the anodic charge transfer α_a is set to 0.5 for most of the time in battery modelling and simulation assuming $\alpha_a + \alpha_c = 1$. Thus, we assume $\alpha_a = \alpha_c = \alpha = 0.5$. From Eq. (11) and (12), the over potential can be derived as [38]:

$$\eta^{\pm}(t) = \frac{RT}{\alpha F}\sinh^{-1}\left(\frac{\mp I(t)}{2a^{\pm}L^{\pm}i_0^{\pm}(t)}\right) \tag{13}$$

where

$$i_0^{\pm}(t) = k^{\pm}\left[c_{ss}^{\pm}(t)\right]^{\alpha} \times \left[c_{e,\mathrm{avg}}^{\pm}\left(c_{s,\max}^{\pm}(t) - c_{ss}^{\pm}(t)\right)\right]^{\alpha} \tag{14}$$

The governing equation of the electrolyte potential is

$$\kappa\frac{\partial\phi_e^{\pm}}{\partial x}(x,t) = -i_e^{\pm}(x,t) + \kappa\frac{2RT}{F}\left(1-t_c^0\right)\times\left(1+\frac{d\ln f_a^{\pm}}{d\ln c_e}(x,t)\right)\frac{\partial \ln c_e}{\partial x}(x,t) \tag{15}$$

Integrating the equation with respect to x across the entire cell width to get [38]

$$\int_{0^-}^{0^+}\frac{\partial\phi_e^{\pm}}{\partial x}(x,t)dx = \int_{0^-}^{0^+}\frac{i_e^{\pm}(x,t)}{\kappa}dx + \int_{0^-}^{0^+}\frac{2RT}{F}\left(1-t_c^0\right)\times\left(1+\frac{d\ln f_a^{\pm}}{d\ln c_e}(x,t)\right)\frac{\partial \ln c_e}{\partial x}(x,t)dx \tag{16}$$

Based on the assumption that the term $\frac{d\ln f_{c/a}^{-}}{d\ln c_e}(x,t)$ is approximately constant in x, the approximation can be made as $1+\frac{d\ln f_{c/a}^{-}}{d\ln c_e}(x,t) \approx k_f(t)$ [38]. Then the expression can be derived as:

$$\phi_e^{+}(t) - \phi_e^{-}(t) = \frac{L^{+}+2L^{\mathrm{sep}}+L^{-}}{2\kappa}I(t) + \frac{2RT}{F}\left(1-t_c^0\right)k_f(t)\left[\ln c_e^{+}(t) - \ln c_e^{-}(t)\right] \tag{17}$$

The solid potential of the electrode can be calculated from the over potential, electrolyte potential, open circuit potential and the solid-electrolyte potential. The expression is

$$\phi_s^{\pm}(t) = \eta^{\pm}(t) + \phi_e^{\pm}(t) + U^{\pm}\left(c_{ss}^{\pm}(t)\right) \tag{18}$$

As the output terminal voltage is a potential difference of the solid potential, the expression is [38]

$$V_t = \phi_s^{+}(t) - \phi_s^{-}(t) \tag{19}$$

From Eq. (13) to (19), the terminal voltage can be expressed as

$$\begin{aligned} V_t = {} & \frac{RT}{\alpha F}\sinh^{-1}\left(\frac{-I(t)}{2a^{+}L^{+}i_0^{+}(t)}\right) - \frac{RT}{\alpha F}\sinh^{-1}\left(\frac{I(t)}{2a^{-}L^{-}i_0^{-}(t)}\right) \\ & + \frac{L^{+}+2L^{sep}+L^{-}}{2\kappa}I(t) + \frac{2RT}{F}\left(1-t_c^0\right)\left[\ln c_e^{+}(t) - \ln c_e^{-}(t)\right] \\ & + U^{+}\left(c_{ss}^{+}(t)\right) - U^{-}\left(c_{ss}^{-}(t)\right) \end{aligned} \tag{20}$$

To solve the partial differential equations, spatial discretisation methods are commonly used, such as finite differences method [32, 33], finite element method [34] and finite volume method [35, 36]. But they usually produce higher-order models. Generally, the higher the order defined in the model, the more accurate the model, but it will greatly increase the computational load. For trade-off between the accuracy and computational cost, the FOM is set with 350th order, where 50th order of positive electrode and 50th order of negative electrode in the solid phase, and 250th order of electrolyte phase, as shown in Fig. 3. The figures of order number are derived from a sensitivity study to balance model accuracy and computational efficiency.

The battery state of charge (SOC) is in relationship with the bulk concentration in steady state. Suppose that the steady-state concentration at 0% and 100% SOC are $\overline{c_{s,0}^{\pm}}$ and $\overline{c_{s,100}^{\pm}}$, respectively. SOC can therefore be presented as:

$$\mathrm{SOC}(t) = \left(\overline{c_s^{\pm}}(t) - \overline{c_{s,0}^{\pm}}\right) \Big/ \left(\overline{c_{s,100}^{\pm}} - \overline{c_{s,0}^{\pm}}\right) \tag{21}$$

2.2. Model order reduction

This FOM is computationally intractable for online implementation. Therefore, model order reduction techniques can be used to reduce the model order while maintaining its accuracy in estimating the cathode and anode potentials. In order to reduce the order of the model, some frequency domain methods can be used to obtain simplified transfer functions to approximate the frequency response of lithium concentration evaluated at the particle surface, such as the Padé approximation algorithm [51] and residue grouping (RG) [52]. RG technique finds the residuals of the spatial distribution by analysing the transfer function and the value and group the residuals with similar eigenvalues to reduce the model order [48]. It therefore accelerates the calculation of the resulting Ordinary Differential Equation (ODE) form of the

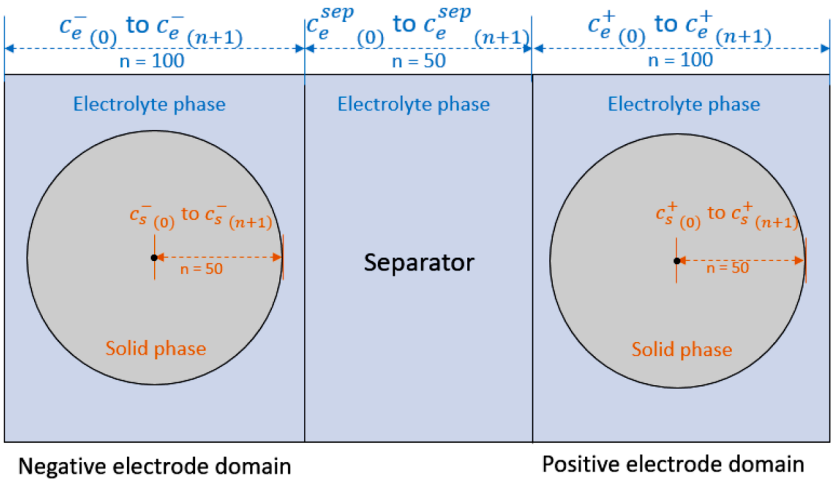

Fig. 3. Schematic of SPMe using FDM in a FOM with 350th orders.

system and performs well in wide frequency ranges. Due to these advantages, RG technology is suitable for model order reduction of Li-ion cell electrochemical models. This paper therefore uses the RG technology to produce the reduced order model of Li-ion cell.

To apply residue grouping method analytically, we must first obtain a transcendental transfer function with an infinite number of poles. Transcendental transfer functions are commonly characterised by numerous closely spaced poles with similar residues. The transcendental transfer function of the positive electrode solid diffusion equation is defined in [48] as:

$$\frac{c_{ss}{}^{+}(s)}{I(s)} = Z + \sum_{k=1}^{\infty} \frac{Res_k s}{s - p_k} \tag{22}$$

where $c_{ss}{}^{+}(s)$ is the surface concentration after Laplace transform, p_k represent the poles, Res_k represent the residues, and Z represents the steady state solution. The poles are [48]

$$p_k = -D_s \left(\frac{\xi_k}{R_s}\right)^2 \tag{23}$$

where ξ_k are roots of $\tan(\xi_k) = \xi_k$ not including $\xi_0 = 0$. The residues are [48]

$$Res_k = \frac{-2}{a_s F R_s p_k} \tag{24}$$

The direct term is

$$Z = \frac{-R_s}{5 a_s F D_s} \tag{25}$$

To balance the simplicity and accuracy of the model, the solid-state diffusion dynamics can be approximated by setting a cut-off frequency of 10 Hz to preserve low-frequency dynamics and ignore high-frequency dynamics above the cut-off frequency [48]. The poles versus residues are plotted in Fig. 4.

Residue grouping method is to partition the frequency range of interest into d "bins" and lump modes within each bin. The grouping procedure yields the D-th order transfer function as a reduced order transfer function. In Fig. 4 the blue dots are the analytical solution of the residues versus poles based on Eq (22). The more grouped points, the higher accuracy and more complex the reduced order model, but the longer computational complexity. Considering both the model accuracy and complexity, the model is reduced to 6 order in the residue grouping method. This is chosen from the result of a sensitivity study to determine the minimum model order with acceptable accuracy comparing with FOM in its normal operating area. Similar model orders are published in [53], that explore comparable studies. After grouping the points into 6 "bins" as shown in the result of Fig. 4, the reduced order solution would be a 6th order transfer function with the input of applied current $I(t)$ and output the solid-state surface concentration of positive electrode, $c_{ss}^{+}(t)$. The same process is repeated on the negative electrode. The transfer function of $\Delta c_e(t)$ vs $I(t)$ can be derived using the method shown in [48, 54].

3. Model linearisation and observer design

3.1. Model linearisation

The terminal voltage, or the over-potential, of the model is a function of electrode solid surface concentration, electrolyte concentration and current. Based on Eqs. (13) to (20), the terminal voltage can be derived as:

$$V(t) = \Delta U(c_{ss}(t)) + \Delta\eta(c_{ss}(t)) + \Delta\phi_e(c_e(t)) + C_o I(t) \tag{26}$$

Thus, the linearisation of the terminal voltage is based on the linearisation of over-potential, $\eta^{\pm}(t)$, positive and negative electrodes open circuit potential (OCP), $U^{\pm}(t)$, and electrolyte potential difference, $\Delta\phi_e(t)$. The linearisation for different parts is based on the same operating points in several regions. The linearisation uses the first order Taylor series expansion approximation technique.

3.1.1. Piecewise linearisation of open circuit potential

In the Li-ion cell, the relationship between lithium concentration in the solid phase at particle surface and corresponding open circuit potential is clearly nonlinear [55]. Normally, the varying of concentration of cathode and anode solid particles are in opposite polarity. During charging the battery, lithium ion is moving from cathode to anode. The lithium concentration in the solid phase of cathode particle is increasing while the lithium concentration in solid phase of anode particle is decreasing. The OCP of cathode and anode are nonlinear functions of the lithium concentration at the electrode surface.

In order to reduce the order of the model and design the observer, its nonlinear function needs to be linearised. The commonly used

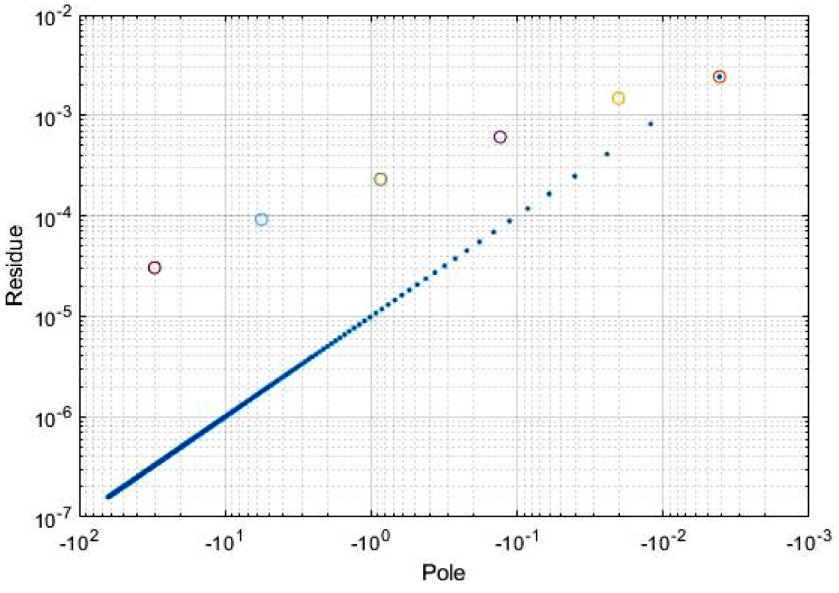

Fig. 4. Solid state diffusion poles and residues: Analytical (.), 6th order grouped (o).

linearisation method is to approximate the nonlinear system based on the linear approximation of the first-order Taylor series near the operating point. But for systems with a very high degree of nonlinearity, the effective area of the linearised model is very limited. When the system operating point deviates from the linearisation point, it will cause a very large deviation between the linearised system and the original nonlinear system. Therefore, for high-order nonlinear systems, a common solution is piecewise linearisation [56], which uses multiple linearisation points to expand the credible space of the simulation results. When the difference between the original nonlinear system and the linearised system is within a specified limit, the linear model is reliable; when the difference exceeds the limit, the next linearisation point will be set [57]. Transition between the different linear regions can be governed by either the SOC of cell or the lithium concentration in electrodes.

The relationship between OCP versus surface lithium concentration in the solid phase of the particle surface is the main nonlinear function in the electrochemical model of Li-ion cell. Since it is a highly nonlinear system, this paper uses piecewise linearisation to linearise the relationship between the OCP and the surface concentration of solid phase. The bulk concentration $\overline{c_s^{\pm}}(t)$ is chosen as the linearisation input for minimising the impact of the nonlinearity. The linearisation of OCP is obtained as:

$$U^{\pm}\left(c_{ss}^{\pm}(t)\right) \approx U^{\pm}\left(\overline{c_s^{\pm}}(t)\right) + \left.\frac{\partial U^{\pm}}{\partial c_{ss}^{\pm}}\right|_{\overline{c_s^{\pm}}(t)} \left(c_{ss}^{\pm}(t) - \overline{c_s^{\pm}}(t)\right)$$
$$= U^{\pm}\left(\overline{c_s^{\pm}}(t)\right) + \left.\frac{\partial U^{\pm}}{\partial c_{ss}^{\pm}}\right|_{\overline{c_s^{\pm}}(t)} \Delta c_s^{\pm}(t) \tag{27}$$

In order to split the whole SOC region into small sub-regions for linearisation, the changing points are chosen at the fastest changing point of first order partial derivatives, or the peak points of second order partial derivatives. The nonlinear reduced order model is linearised to the average gradient within the related operating region. As the battery SOC has a linear relationship with the bulk concentration as given in (21), either the bulk concentration or battery SOC from the linear model can be used for switching the sub-regions.

In this paper, the LGM50 cell is chosen as the target cell. The M50 is a type of 21,700 cylindrical cell produced by LG Chem, which is widely studied in previous research [55, 58, 59]. The parameter sets of open circuit potentials are from the experimental data published in [7]. The relationship between lithium concentration in the solid phase at particle surface $c_{ss}^{\pm}(t)$ and corresponding open circuit potential $U^{\pm}(t)$ is shown in Fig. 5. The linearised open circuit potential of cathode particle based on (27) and its partial derivatives of open circuit potential to surface concentration of solid phase is shown in Fig. 5(a) and (c), while that of anode particle is shown in Fig. 5(b) and (d). In total, the whole region when SOC changes from 0 to 100% has been divided into 8 sub-regions in the cathode and anode, respectively. This is chosen as the minimum number of sub-regions to present the nonlinear behaviour of open circuit potential of this type of cell.

Fig. 5 shows the accuracy of the piecewise linearisation result of the cathode and anode potential versus the lithium concentration on surface of solid phase compared with the nonlinear function. The coefficient of determination of the fitting function is equal to 0.99986, which shows that even when the battery is in a highly dynamic state, the operating point of the linearised system is still not far away from the static operating point. This ensures the effectiveness of the system based on piecewise linearisation in the full working range.

3.1.2. Over-potential linearisation

The over-potential in Eq (13) takes the current as the input. An approximation can be made with $\sinh^{-1}(x) \approx x$. The over-potential can be simplified to have the linear relationship with current as defined by:

$$\Delta\eta = \eta^{+} - \eta^{-} = \frac{RT}{\alpha F}\left[\sinh^{-1}\left(-\frac{I(t)}{2a^{+}L^{+}i_0^{+}(t)}\right) - \sinh^{-1}\left(\frac{I(t)}{2a^{-}L^{-}i_0^{-}(t)}\right)\right]$$
$$\approx -\frac{RT}{\alpha F}\left(\frac{1}{2a^{+}L^{+}i_0^{+}(t)} + \frac{1}{2a^{-}L^{-}i_0^{-}(t)}\right) I(t) \triangleq R_{nl}(t) I(t) \tag{28}$$

It is noteworthy that R_{nl} defined in Eq (28) depends on $i_0^{\pm}(t)$, which is a function of the solid and electrolyte concentration as given in Eq (14). $i_0^{\pm}(t)$ is a function of the surface concentration.

3.1.3. Electrolyte potential linearisation

The electrolyte concentration in Eq (8) is linearised at the average electrolyte concentration ($\overline{c}_e$),

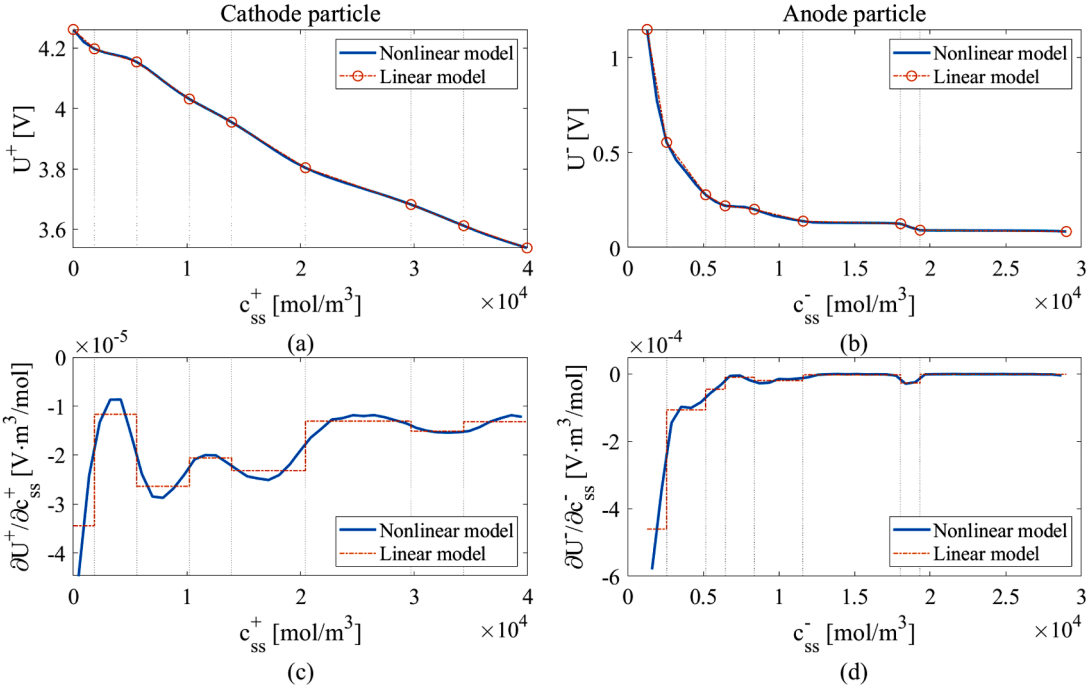

Fig. 5. Piecewise linearisation of OCP versus electrode solid surface concentration for different operating regions in cathode and anode particles.

$$k_{conc}[\ln(c_e(0^+,t)) - \ln(c_e(0^-,t))] \approx k_{conc}\frac{c_e(0^+,t) - c_e(0^-,t)}{\overline{c}_e} \tag{29}$$

Thus,

$$\phi_e^+(t) - \phi_e^-(t) = \frac{L^+ + 2L^{sep} + L^-}{2\kappa} I(t) + \frac{2RT}{F}\left(1 - t_c^0\right)\frac{c_e(0^+,t) - c_e(0^-,t)}{\overline{c}_e} \tag{30}$$

3.1.4. Linearisation of the reduced order model

Overall, the concentration of $c_{ss}^{\pm}(t)$ and $\Delta c_e(t)$ are presented in state variable form after model order reduction. The state-space function is shown as:

$$\dot{\boldsymbol{X}} = \boldsymbol{A}\boldsymbol{X} + \boldsymbol{B}u \tag{31}$$

where u is the input current $I(t)$. $\boldsymbol{X}$ is the state vector defined based on the 16th order ROM, which contains 7 states for positive solid particle, 7 states for negative solid particle and 2 states for electrolyte. The states vector $\boldsymbol{X}$ is defined as

$$\boldsymbol{X} = [\overline{c_s^+} \quad c_{s1}^+ \quad c_{s2}^+ \quad c_{s3}^+ \quad c_{s4}^+ \quad c_{s5}^+ \quad c_{s6}^+ \quad \overline{c_s^-} \quad c_{s1}^- \quad c_{s2}^- \quad c_{s3}^- \quad c_{s4}^- \quad c_{s5}^- \quad c_{s6}^- \quad c_e^+ c_e^-]^T \tag{32}$$

The state matrix $\boldsymbol{A}$ and $\boldsymbol{B}$ contain the lumped values that are calculated from the Matlab linearisation toolbox as

$$\boldsymbol{A} = \begin{bmatrix} \boldsymbol{A}_+ & & \\ & \boldsymbol{A}_- & \\ & & \boldsymbol{A}_e \end{bmatrix} \tag{33}$$

where

$$\boldsymbol{A}_{\pm} = \begin{bmatrix} 0 & 0 & 0 & 0 & 0 & 0 & 0 \\ 0 & & 1 & & & & \\ 0 & & & 1 & & & \\ 0 & & & & 1 & & \\ 0 & & & & & 1 & \\ 0 & & & & & & 1 \\ 0 & a_1^{\pm} & a_2^{\pm} & a_3^{\pm} & a_4^{\pm} & a_5^{\pm} & a_6^{\pm} \end{bmatrix} \tag{34}$$

$$\boldsymbol{A}_e = \begin{bmatrix} a_1^e & 0 \\ 0 & a_2^e \end{bmatrix} \tag{35}$$

and

$$\boldsymbol{B} = [b_1^+ \quad 0 \quad 0 \quad 0 \quad 0 \quad 0 \quad b_2^+ \quad b_1^- \quad 0 \quad 0 \quad 0 \quad 0 \quad 0 \quad b_2^- \quad b_1^e \quad b_2^e]^T \tag{36}$$

where a_j^+ and a_j^- $(j = 1, 2, \cdots, 6)$ are the state parameters of lithium concentration of cathode (+) and anode (-) solid phase in its jth order states, respectively; a_1^e and a_2^e are the parameters of electrolyte; b_1^+, b_2^+, b_1^-, b_2^-, b_1^e and b_2^e are the parameters of input current that affect the states.

The output vector $\boldsymbol{Y}$ is defined

$$\boldsymbol{Y} = [c_{ss}^+ \quad c_{ss}^- \quad \phi_s^+ \quad \phi_s^- \quad V_t]^T \tag{37}$$

The output matrix is obtained from the previous Eqs. (26) to (30) and its values are calculated in the Matlab toolbox providing a numerical solution but with no clear physical meaning. The validation between linear and non-linear model are given in Section 4.

3.2. Full-order Luenberger observer design

The behaviour of the linearised ROM can be represented by an approximate linear system that satisfies the superposition property. With that, a linear observer can be designed to estimate the states and dynamics of Li-ion battery system. The Luenberger observer is a full-order observer, which is used to process the state estimation of linear deterministic dynamic systems. Compared with the Kalman filter, the Luenberger observer may be more sensitive to onset of external disturbances and uncertainty. In the full-order Luenberger observer design, the estimation error of the terminal voltage is used as the feedback to drive the observer to track the state dynamics of the lithium-ion battery system, as shown in Fig. 6. The parameter matrix is from the linearised system discussed in the above section.

With the target linear system model in (31) and system output in (37), the outputs of the linearised system and observer of Li-ion battery includes 5 variables. But in the real battery, the only feedback is the system output y_5, namely the terminal voltage V_t. The full-order Luenberger observer can be designed with adding a term of output error with a linear gain in the state function as

$$\begin{aligned} \dot{\widehat{\boldsymbol{X}}} &= \boldsymbol{A}\widehat{\boldsymbol{X}} + \boldsymbol{B}u + \boldsymbol{L}(y_5 - \widehat{y}_5) \\ \widehat{y}_5 &= \boldsymbol{C}\widehat{\boldsymbol{X}} + \boldsymbol{D}u \end{aligned} \tag{38}$$

as the state error is defined as: $\widetilde{\boldsymbol{X}} = \boldsymbol{X} - \widehat{\boldsymbol{X}}$. The error function can be obtained by the difference between (31) and (38) as $\dot{\widetilde{\boldsymbol{X}}} = [\boldsymbol{A} - \boldsymbol{L}\boldsymbol{C}]\widetilde{\boldsymbol{X}}$. Then the convergence rate of estimation error can be obtained as

$$\widetilde{\boldsymbol{X}}(t) = e^{[\boldsymbol{A}-\boldsymbol{L}\boldsymbol{C}]}\widetilde{\boldsymbol{X}}_0 \tag{39}$$

The estimation error at time t is converged exponentially from initial error $\widetilde{\boldsymbol{X}}_0$.

In the linearised Li-ion battery system, the parameter matrix $\boldsymbol{A}$ and $\boldsymbol{C}$ are fixed in each operating region. The poles of matrix $[\boldsymbol{A} - \boldsymbol{L}\boldsymbol{C}]$ are obtained using pole placement to ensure the convergence speed by adjusting the value of the observer gain $\boldsymbol{L}$. In the classical Luenberger observer, the observer gain is designed with its pole in proportional to the pole of the system [60]. In the observer, the gain $\boldsymbol{L}$ is a $[16 \times 1]$ vector for the state vector $\boldsymbol{X}$ of the 16th order ROM. Thus, the value of $\boldsymbol{L}$ is selected based on the range of states in $\boldsymbol{X}$. Ideally, the higher the control gain in L, the better the estimation performance of observer (faster convergence and reduced steady state error). But this would come at the expense of increasing the sensitivity of the system to higher frequency noise and uncertainty. In order to balance between the convergence speed of observer output and sensitivity to sensor noise and uncertainty, the observer gain is chosen to keep the observer bandwidth wider than the frequencies of system dynamic and narrower than the sensor noise. The turning of observer parameters is based on the integrated absolute error (IAE) of estimation of the cathode and anode OCP

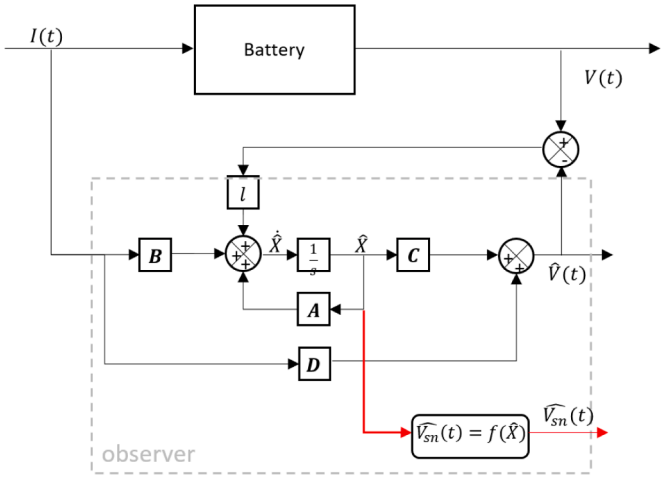

Fig. 6. Block diagram of the Luenberger observer.

under the disturbance of a step changed terminal voltage error. The observer gain is chosen to minimise the IAE of estimation in order to ensure the fast convergence of estimation error and avoid the system unstable due to the error accumulation over time.

In addition, it is necessary to select the optimal value by adjusting the gain $\boldsymbol{L}$ of the observer in each sub-interval since the observer is designed based on the combination of multiple linear models by the piecewise linearisation of the nonlinear system. The selection of the observer gain $\boldsymbol{L}$ is optimised in each interval separately to ensure that the observer is in the optimal state in each independent subinterval. In practice, when the system switches between different regions, the observer gain, $\boldsymbol{L}$, is also varying depending on the changing within the system matrix. This aims to ensure that the observer has the same convergence speed and dynamic response across the whole SOC region of the battery. Therefore, in each interval, the tuned parameters of observer can ensure the convergence of the estimation error in the interval and the stability of the system.

In the designed observer, the switching condition is based on either the estimated surface lithium concentration or the SOC. They are variables that are changing continuously. Assuming that in the interval before switching, the gain $\boldsymbol{L}$ of the observer has ensured the convergence and stability of the system. When the observer switches to another interval parameters, the estimation error will not jump due to the switching of the observer gain $\boldsymbol{L}$. Therefore, the switching of the observer gain $\boldsymbol{L}$ will not affect the stability of the observer.

4. Model parameterisation and validation

4.1. Experiment set-up and model parameterisation

In order to deconvolute the electrochemical behaviour of the positive electrode and negative electrode, three-electrode configurations of the LGM50 cell were used. The cylindrical cell was disassembled, and the electrodes were harvested to be used in a three-electrode PAT-Cell, as shown in Fig. 7. The cylindrical cell was discharged to 2.5 V (as 0% SOC defined by the manufacturer) at C/50 and transferred to an argon glovebox environment to extract the electrodes and disassembled following the best practice. After disassembling the cylindrical cell, the positive and negative electrodes were soaked in dimethyl carbonate (DMC) overnight to remove electrolyte residues, and vacuum dried at 50 °C for construction a later time. It is necessary to keep one side of the electrode intact during the cleaning process. This teardown procedure is described in detail in our previous published papers [7].

The three-electrode test is performed using PAT-Cells. The cells were composed of extracted positive electrode of NMC and a negative electrode of graphite-SiOx both with a diameter of 18 mm. In the three-electrode arrangement, the negative electrode and the positive electrode are assembled with a third reference electrode to achieve deconvolution of individual electrode potentials. In order to operate a stable reference electrode, the cell configuration requires electrochemical and physical symmetry [7]. In the PAT-Cell used in this paper, a lithium ring reference electrode is used to clarify the potential of each electrode. Other components include a 21.6 mm diameter double-layer separator comprised of a180μm woven polypropylene layer and a 38 μm polyethylene membrane. 100 μl of electrolyte was used, this contained $1\mathrm{mol/dm^{-3}}$ $LiPF_6$ in ethylene carbonate: ethyl methyl carbonate (3:7, v:v, Soulbrain). The model parameters used have been measured previously during the experimental evaluation of the LGM50 [7], modified to

Table 1
Parameters of SPMe model measured from PAT-Cell.

Parameters	Symbol	Value
Thickness of cathode	L^{+}	75.6 μm
Thickness of separator	L^{sep}	12 μm
Thickness of anode	L^{-}	85.2 μm
Radius of solid particles in cathode	R_s^{+}	5.22 μm
Radius of solid particles in anode	R_s^{-}	5.86 μm
Volume fraction of solid in cathode	ε_s^{+}	0.547
Volume fraction of solid in anode	ε_s^{-}	0.693
Volume fraction of electrolyte in cathode	ε_e^{+}	0.335
Volume fraction of electrolyte in separator	$\varepsilon_e^{\mathrm{sep}}$	0.47
Volume fraction of electrolyte in anode	ε_e^{-}	0.25
Diffusion coefficient of solid in cathode	D_s^{+}	0.0025 $\mu\mathrm{m}^2/\mathrm{s}$
Diffusion coefficient of solid in anode	D_s^{-}	0.007 $\mu\mathrm{m}^2/\mathrm{s}$
Diffusion coefficient of electrolyte	D_e	177 $\mu\mathrm{m}^2/\mathrm{s}$
Conductivity of solid in cathode	σ^{+}	10 /Ωm
Conductivity of solid in anode	σ^{-}	100 /Ωm
Bruggeman porosity	b	1.5
Ambient temperature	T	298.15 K
Transference number	t_{c0}	0.363
Kinetic reaction rate of cathode	k^{+}	$3.42 \times 10^{-6}(\mathrm{A/m^2})(\mathrm{mol/m^3})^{-1.5}$
Kinetic reaction rate of anode	k^{-}	$6.48 \times 10^{-7}(\mathrm{A/m^2})(\mathrm{mol/m^3})^{-1.5}$
Charge transfer coefficients	α	0.5 Ω/m^2
Thermal conductivity	κ	1.05 $W/\mathrm{m{\cdot}K}$
Faraday's constant	F	96,485 C/mol
Universal gas constant	R	8.314 J/mol·K
Fixed electrolyte concentration	c_e	1000 $\mathrm{mol/m^3}$
Cell maximum voltage	$V_{\max}$	4.2 V
Cell minimum voltage	$V_{\min}$	2.5 V
Maximum concentration of cathode	$c_{s,\max}^{+}$	41,800 $\mathrm{mol/m^3}$
Maximum concentration of anode	$c_{s,\max}^{-}$	32,593 $\mathrm{mol/m^3}$

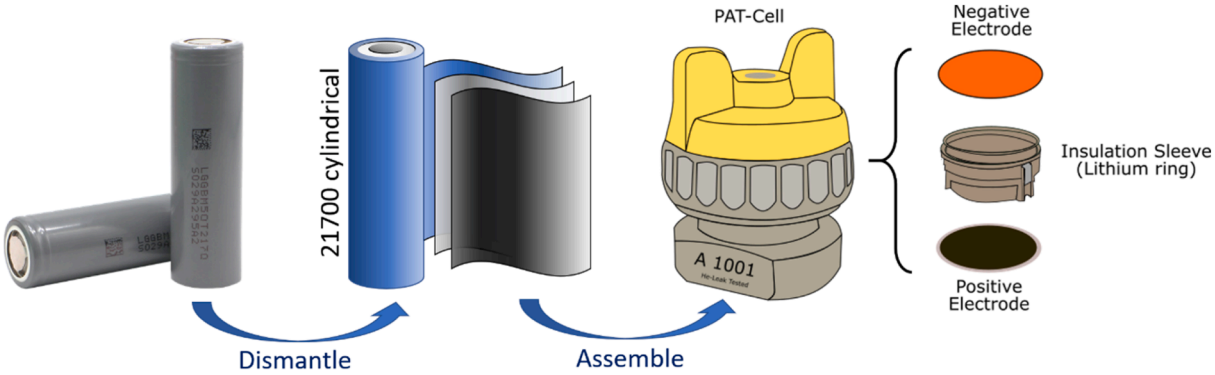

Fig. 7. Illustration of the tear-down method used to extract electrodes from a cylindrical cell into a three-electrode PAT-Cell.

account for the PAT-Cell configuration. This paper uses the same approach for parameterisation and the model parameters are given in Table 1 with a full description of the test methodology provided in [7].

In this paper, it is assumed that most parameters of the commercial cell are the same with that of the PAT-Cell, such as the thickness of negative and positive electrodes, reaction rates, transport parameters, diffusion coefficient, conductivity, kinetic parameters, and thermodynamic parameters, as given in Table 1. The only differences between the original cell and PAT-Cell are the electrodes area (or capacity), thickness of separator and electrolyte.

Before electrochemical testing, the cells underwent an SEI formation step of two C/20 cycles between 2.5 V and 4.2 V, during the constant current – constant voltage (CC—CV) charge the current cut-off was C/50. The testing involved charging with a CC—CV at a charge rate of 0.3C, 0.5C and 1C until 4.2 V voltage and the cut-off current of C/50. After charging is completed, there was an OCP period of 1 hour to allow the cell to equilibrate, before the cell was discharged to 2.5 V with a constant current of 0.5C, 1C and 2C. In the test, the PAT-Cell has the electrodes of the original battery, the potential of its cathode and anode can be measured in real time in a laboratory environment. Before the drive cycle was undertaken (discussed further in Section 5.2) the cells were charged to 4.2 V followed by an OCP step of 1 hour to provide stable initial conditions for the model, the drive cycle was applied till a voltage of 2.5 V was reached.

4.2. Model validation

In previous section, the observer is designed based on the reduced-order SPMe model of Li-ion battery. Before testing the performance of the observer, the reliability of different battery model needs to be validated with the experiment. The FOM with 350th order, ROM with 16th order, and LM based on the ROM are compared with the three-electrode experimental data. The validation compares the experiment result with the FOM, ROM and LM in CC—CV charging with 0.3C, 0.5C, 1C and 2C current rate and constant current (CC) discharging with 0.1C, 0.3C, 0.5C, 1C and 2C current rate. In order to show the result clearly, the curves of cathode and anode potential during CC—CV charge at 0.5C and CC discharge at 0.5C are given in Fig. 8 and Fig. 9, respectively.

In the result of CC—CV charge at 0.5C, all the models are applied with the same constant charging current as within the experiment. The model validation is using its own CC—CV charging logic. The switching logic from constant current (CC) to constant voltage (CV) is the same, that is, when battery terminal voltage reaches 4.2 V. Thus, in different model, the switching point is slightly different. The cathode potential and anode potential of all models track the real value from the experiment in both the CC and CV charge stages. The enlarged figures show the cathode and anode potential at the point of switching from CC to CV. In the result, Fig. 8(a) shows the charging current in its C rate. The FOM is the first that matches the voltage upper limit while the LM model is the last. In the result of CC discharge at 0.5C, the models have similar performances but have relatively increased error with experimental result than that in the charging cycle.

In the whole discharging period, the FOM performs the best in terms of emulating both cathode potential and anode potential estimation compared with the experimental data. In order to show the detailed comparison, the root mean square error (RMSE) of cathode and anode potential at different charging/discharging C rate is summarised in Table 2.

In the RMSE comparison, the positive C rates indicate the constant current in CC—CV charging and negative C rates indicate the peak current in CC discharging of the cell. The result in Table 2 also gives the estimation error in RMSE of different current rates. To aid understanding the RMSE result of different C rate is shown in the bar chart of Fig. 10, where (a) and (b) show the RMSE error of cathode and anode potential estimation in CC—CV charge while (c) and (d) show that of CC discharge. The result shows that the FOM matches the experimental data

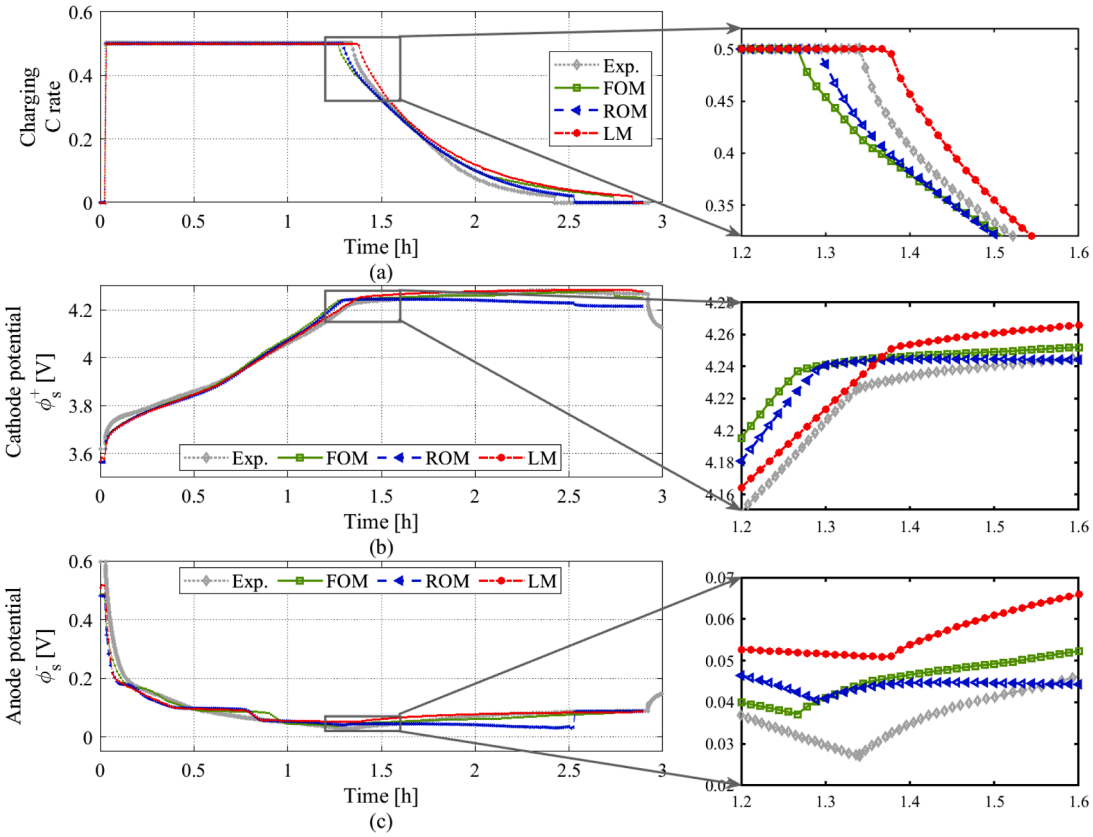

Fig. 8. Model validation of comparing experiment, FOM, ROM and LM on cathode and anode potential during CC—CV charge.

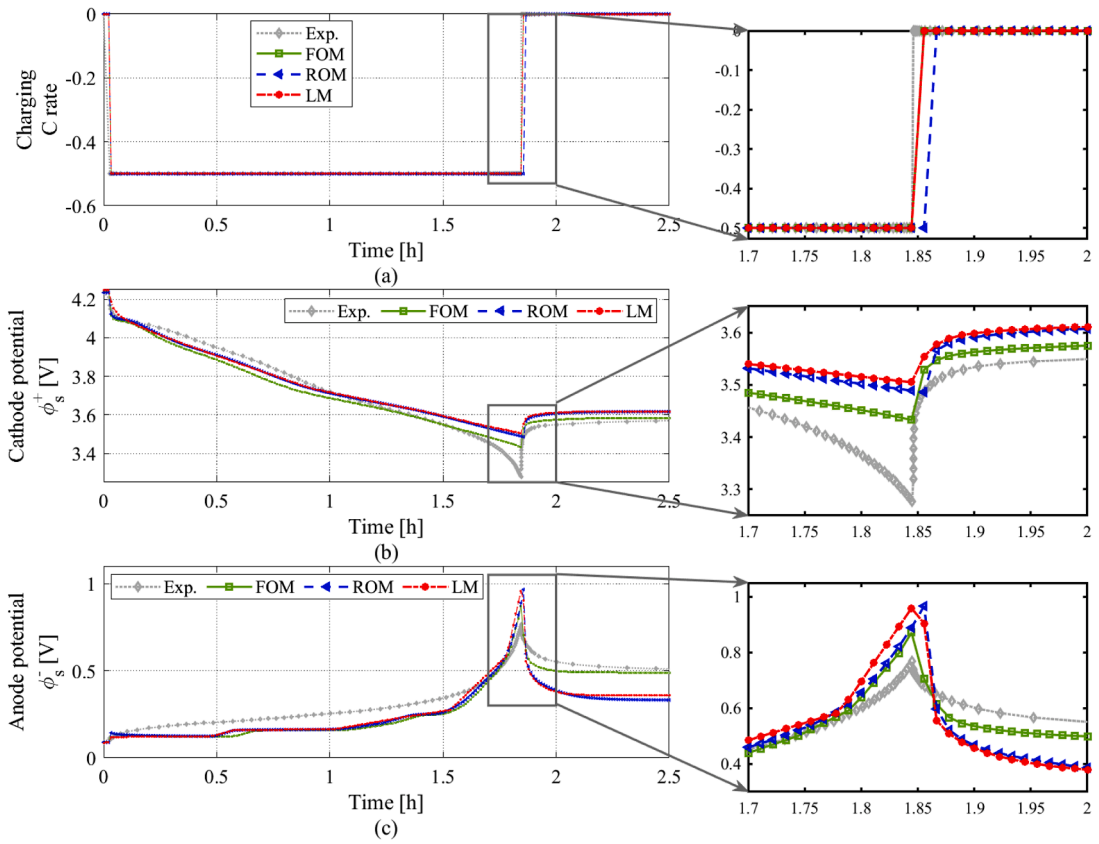

Fig. 9. Model validation of comparing experiment, FOM, ROM and LM on cathode and anode potential during CC discharge.

Table 2
RMSE of model validation at different C rate.

Current rate	FOM		ROM		LM	
	$\Delta\overline{\phi}_s^+$ [V]	$\Delta\overline{\phi}_s^-$ [V]	$\Delta\overline{\phi}_s^+$ [V]	$\Delta\overline{\phi}_s^-$ [V]	$\Delta\overline{\phi}_s^+$ [V]	$\Delta\overline{\phi}_s^-$ [V]
0.3C	0.0157	0.0501	0.0284	0.0562	0.0357	0.0687
0.5C	0.0181	0.0211	0.031	0.0325	0.0298	0.0313
1C	0.0252	0.0356	0.0345	0.0366	0.0332	0.0361
2C	0.0306	0.027	0.0392	0.0343	0.0389	0.0352
−0.1C	0.0161	0.0379	0.028	0.0967	0.0298	0.0969
−0.3C	0.0314	0.0394	0.0374	0.0847	0.0403	0.0884
−0.5C	0.0434	0.067	0.0501	0.1056	0.0538	0.1117
−1C	0.0395	0.1588	0.0621	0.1502	0.0649	0.1578
−2C	0.0954	0.18	0.0958	0.1749	0.1395	0.165

well in charging and low current discharging. When the FOM applied for discharging in a C rate higher than 2C, the estimation error increases to nearly 0.1 V. The reason can be the limit of FDM method and the number of model order in the FOM. The ROM method performs worse than the FOM in most C rates. The LM model performs similar with the ROM in most cases that validates the method of linearisation employed.

Even though the LM has the relatively large error, compared to the FOM derivative, especially in discharging cases, it has the fastest operating speed than the FOM and ROM models, as highlighted in the comparison in Table 3. The result shows the simulation time of different models using the same PC hardware with the CPU of Intel Core i7–8650 U at 2.11 GHz and 16.0GB RAM. The chosen of simulation time step considers all three models. Generally, the shorter the simulation step, the more accurate the model will run. If the time step is too long, the model will not be able to track the actual value in time, and thus causing larger quantisation error and potentially numerical instability. If the time step is too short, the calculation time of FOM will be very long, which is not suitable for real-time operation. In addition, the purpose of the observer design is to be applied to the embedded digital signal processor (DSP) in the BMS in the future. The computing power of DSP is much lower than that of a general CPU. Thus, the chosen of simulation step size also needs to consider the simulation effect of each model under the condition of lower computing power. Considering these situations comprehensively, this paper chooses the simulation time step to be 0.1 s, and uses the same simulation step in FOM, ROM and LM.

For example, in a 2C discharge rate, the experiment will take about 30 min to discharge the cell from full to zero. In the simulation, the FOM requires about 6 min to simulate the whole process while the ROM and LM require only 6.8 s and 4.5 s, respectively. In average, the simulation time of FOM is 105 times longer than the LM and 50 times longer than the ROM. This verifies that the LM reduces the computational cost by circa: 52% compared to the ROM model and 99% compared to the FOM model. Therefore, the LM is the most suitable model used for the observer design for the purpose of charging/discharging control in real-time applications.

5. Observer performance investigation

The previous section validates the FOM, ROM and LM model formulations with experiment data. All the models are operating separately. This section validates the observer that can compensate the gap between reference and estimated outputs. The observer aims to estimate the cathode and anode potentials of battery cells using the measured terminal voltage and applied current. To investigate the observer performance, different use cases are studied.

5.1. Observer test with battery model

In previous test, the battery model is able to emulate the dynamic

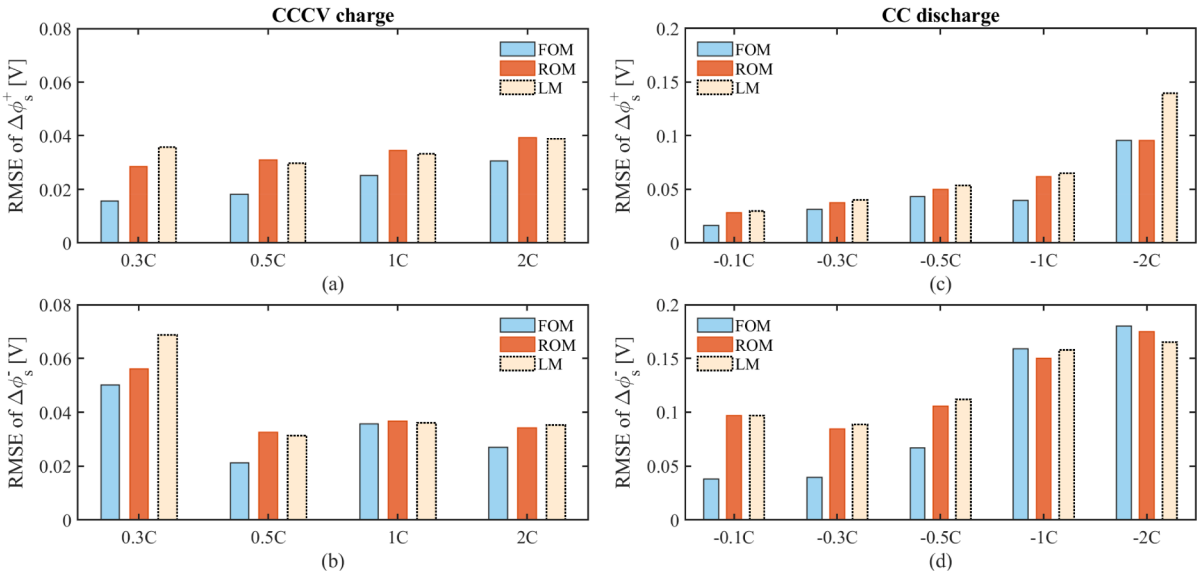

Fig. 10. RMSE value of cathode and anode potential in model validation amongst FOM, ROM and LM.

Table 3
Model simulation time comparison.

Current rate	2C discharge	1C discharge	0.5C discharge	0.3C discharge	0.1C discharge
Experiment	~0.5 hrs	~1.5 hrs	~2.5 hrs	~4 hrs	~10 hrs
FOM	338.8 secs	981.74 secs	1563.9 secs	2560.3 secs	6187.3 secs
ROM	6.79 secs	18.87 secs	32.62 secs	48.18 secs	120.1 secs
LM	4.51 secs	10.25 secs	14.96 secs	21.6 secs	47.37 secs

response of a real cell, and FOM performs the best in all of the three models. In this subsection, the FOM is used as a proxy for a real battery to allow us to expand the scope of the investigation. The first use-case is to test the observer performance when used in simulation with the FOM based battery plant model.

In the case study, the same current profile is applied to the battery plant model and observer. Only the terminal voltage from the FOM based battery plant model is used as a feedback to the observer. The estimated concentration and potential of cathode and anode from the observer is compared with its real value from the battery plant model. The test of battery charging uses CC—CV strategy with 0.3C, 0.5C and 1C current rate from 0% SOC. The simulation result is shown in Fig. 11.

In the result, the observer states are driven by the applied current and estimation error of the terminal voltage until the estimated terminal voltage tracks its real value, as shown in Fig. 11(b). The observer dynamics include 16 states and 5 outputs, including the surface concentration and potential of solid phase in cathode and anode particles. The estimation performance of these four states in 0.3C, 0.5C and 1C charge are compared with the real value from the FOM based battery plant model, which is used as a proxy for the real battery, as shown in Fig. 11 (c) to (f). The result shows that the tracking error of CC charging period performs better than the CV charging phase. And the result of cathode and anode potential estimation with 0.3C has less error than that with 0.5C and 1C. The error is caused by the mismatch between the nonlinear model and linear model-based observer. The detailed estimation performance in numerical comparison is given in Table 4.

Apart from the CC—CV charging test, the observer performance is evaluated in CC discharge. The discharging current is set to −0.5C, −1C and −2C to discharge the cell from 100% SOC. The estimation performance comparing the non-linear battery model and linear model-based observer is shown in Fig. 12. Same with the charging cases, the surface concentration and potential of the solid phase in cathode and anode particles are compared. The result shows that the estimated cathode and anode potential from the observer tracks well the real value derived from the full order plant model.

5.2. Observer experimental validation

In this section, the observer estimation performance is evaluated with experimental data from the PAT-Cell characterised in Section 4.1 and reported in [7]. The main difference of this test with the one discussed in the previous section is that the real battery is much more complex than a battery model and thus includes more uncertainties to the observer. The applied current use the same current density. The error of terminal voltage is used to drive the observer states in order to compensate for the difference between observer and real cell.

When verifying the designed observer with experimental data, the current input and terminal voltage feedback of the observer are obtained in real time from the experiment of PAT Cell. Due to the three-electrode property of the PAT Cell, its positive and negative potentials can be measured in real time in a laboratory environment. However, the positive and negative potentials measured from PAT Cell will not participate in any calculations in the observer, and are only used for comparison with the estimated positive and negative potentials of the observer.

Since the PAT Cell uses electrodes harvested from a disassembled cylindrical cell, the capacity of the PAT Cell is much smaller than that of original cylindrical cell. The electrode area of the PAT cell is 2.54cm^2 while that of cylindrical cell is 1027cm^2. The capacity of LGM50 cell is determined to be 4.5mAh/cm^2 for positive electrode in our previous study of model parameterisation [7]. Thus, the 1C for the PAT-Cell is about 11.4 mA. In order to unify the current applied between the PAT-Cell and the model of original cylindrical cell, the current applied to the PAT-Cell needs to be converted to the corresponding current with the same current density based on the capacity or positive electrode area, and then input this value to the observer. Thus, after the conversion, the 1C current rate of the original cylindrical cell is approximately 4.62A.

The observer performance test with real experimental data in 0.3C, 0.5C and 1C CC—CV charging from 0% initial SOC is shown in Fig. 13. As the concentration is not available to be directly measured in the experiment, the result only validates the estimated cathode and anode potential with the measured value in the experiments. The results show that the estimated cathode and anode potential tracks the real value well

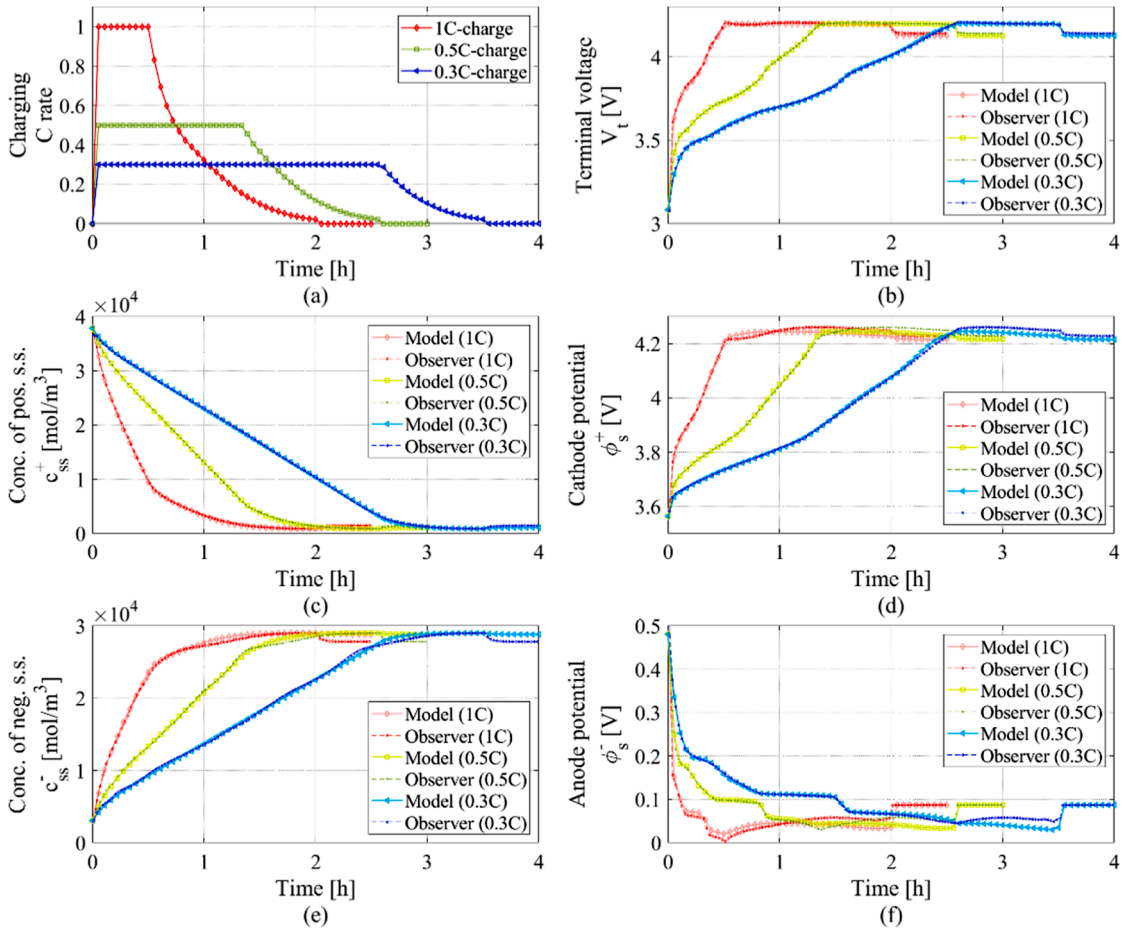

Fig. 11. Simulation of observer estimation performance with FOM based battery plant model under CC—CV charge at different C rate. a) Applied current C rate; b) Terminal voltage; c) Surface concentration of solid particle in positive; d) Cathode potential; e) Surface concentration of solid particle in negative; f) Anode potential.

Table 4
RMSE of observer estimation error.

Current rate	Model		Experiment	
	$\Delta\widehat{\phi}_s^+$ [V]	$\Delta\widehat{\phi}_s^-$ [V]	$\Delta\widehat{\phi}_s^+$ [V]	$\Delta\widehat{\phi}_s^-$ [V]
0.3C	0.0108	0.0086	0.0147	0.0193
0.5C	0.0123	0.0102	0.0163	0.0147
1C	0.0142	0.0124	0.0177	0.0163
−0.5C	0.0044	0.0065	0.0499	0.0515
−1C	0.0068	0.0065	0.0491	0.0626
−2C	0.027	0.0364	0.0402	0.0756

but with its estimation error larger than that with battery model in previous case study, which is to be expected. The error caused by the difference between battery model with the real cell. Even though the model cannot provide the exact same dynamics as the real cell, the observer is able to compensate for these differences by tracking the terminal voltage. Therefore, when there is no error between the estimated terminal voltage and feedback from the real battery in the experiment, the cathode and anode potential track their real value.

As in Fig. 13, the estimation error of observer can underestimate the lithium plating. This issue can be solved in practice by increasing the warning threshold of low anode potential detection in BMS. In the electrochemical experiments of Li-ion batteries, 0.005 V is selected as full lithiation limit of the negative electrode, as lower anode potential will cause lithium plating and dendrites [7]. However, in practice, the lower limit of the anode potential can be increased to provide redundant space for estimation errors. For example, if the anode potential limit is set to 0.02 V, the BMS will request a reduction in the charging current when it detects that the estimated anode potential by observer is less than 0.02 V. This can bring 0.015 V space for estimation error to avoid lithium plating.

In the observer performance test during CC discharging, the discharging current is chosen with 0.5C, 1C and 2C, as shown in Fig. 14, and the initial SOC of target cell is 100% fully charged. Same with the charging test, only the estimated cathode potential and anode potential are compared with their measured values. In the discharging test, the estimation error of both the cathode potential and anode potential is greater than that in the charging test. This result is aligned with the previously reported model validation result. With tracking the terminal voltage via reducing its error, the estimated cathode potential and anode potential are able to track their measured values. In order to compare the observer performance with more details, the detailed numerical result of estimation in both the charging and discharging cycles is given in Table 4.

The result shows the observer estimation error to model and experiment for different C rates. However, in the same current C rate, the observer is able to eliminate the error of the cathode and anode potential comparing with the model itself. For example, in the 0.3C CC—CV charge, the LM has the RMSE of cathode and anode potential with experiment result with 0.0179 V and 0.0491 V as shown in Table 3 while with the observer eliminating the error of terminal voltage, the RMSE of cathode and anode potential estimation error reduced to 0.0147 V and 0.0193 V. On average, the observer can reduce more than 20% error in the cathode potential estimation and 50% error in anode potential estimation caused by the uncertainty between the battery model and

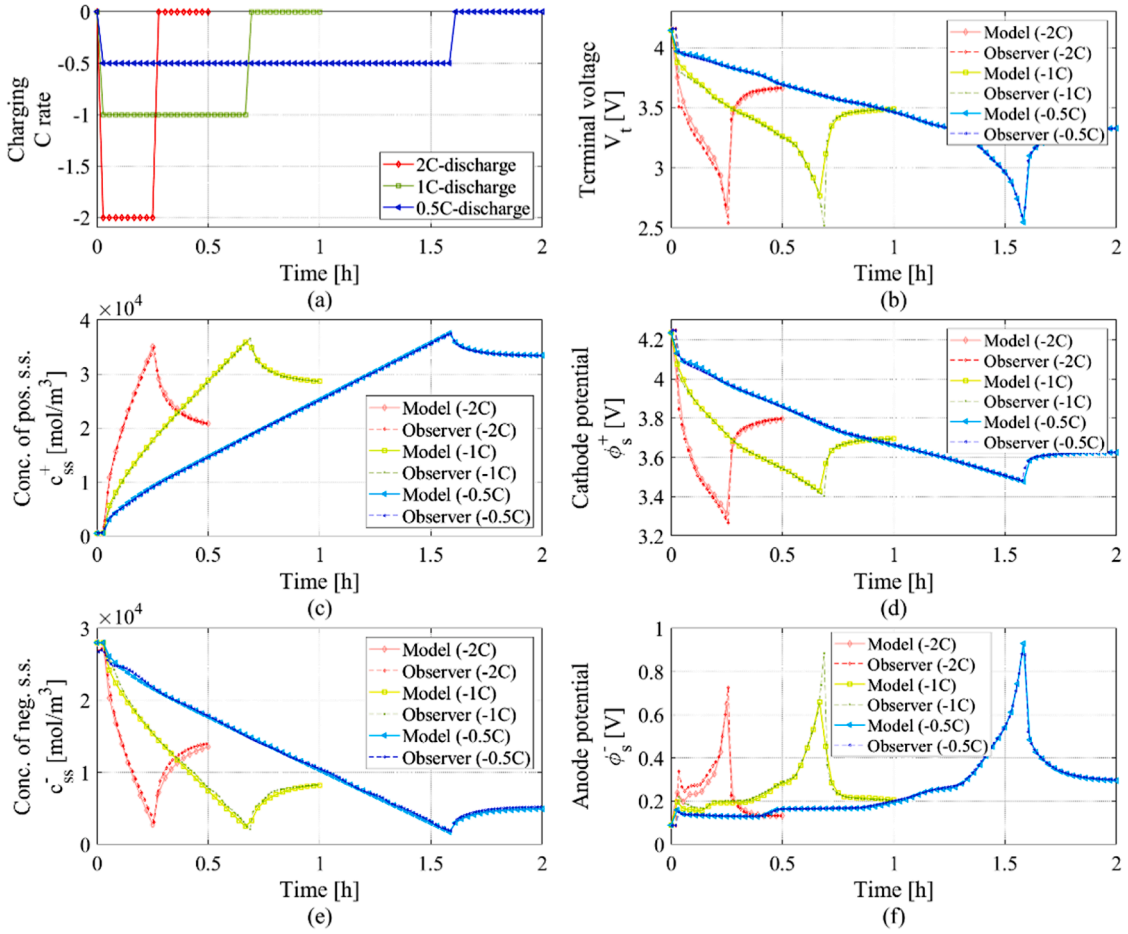

Fig. 12. Simulation of observer estimation performance with FOM based battery plant model during CC discharge with different C rate. a) Applied current C rate; b) Terminal voltage; c) Surface concentration of solid particle in positive; d) Cathode potential; e) Surface concentration of solid particle in negative; f) Anode potential.

real cell. In order to show the result clearly, the result in Table 4 is presented in Fig. 15.

5.3. Observer test with real-world drive cycle

In electric vehicle (EV) applications, the rapidly changing current caused by frequent regenerative braking may bring the risk of low anode potential. Therefore, in this case, the observer was tested with a three-electrode PAT-Cell under a real-world drive cycle.

In order to make the results more universal and representative, a standardised test cycle should be selected from the vehicle driving profile. The New European Driving Cycle (NEDC) is one of the test cycles widely used in vehicle driving tests. It consists of two parts: an urban driving cycle and an extra urban driving cycle [61, 62]. NEDC includes four operating conditions, including acceleration, deceleration, constant speed and idling conditions, so it can reflect the actual operating conditions of real vehicles [62]. In this article, the driving cycle used for testing the Li-ion cell is derived from a simple EV powertrain model and a sample driving profile from NEDC. The total running time of the NEDC is 1180s. Therefore, the current cycle of charging/discharging for the PAT-Cell is obtained by repeating the NEDC curve until the battery discharges to its lower limit.

At the start of the test, the PAT-Cell is fully charged to 100% SOC. This test aims to validate the observer performance in real-worlduse cases including frequent charging/discharging cycles rather than an ideal CC discharging. The result is shown in Fig. 16.

The test takes about 6.5 h until the terminal voltage reaches 2.5 V. To show the result clearer, a part of the result is chosen and enlarged to find the estimation performance of the observer. The result shows that the observer estimates cathode and anode potential and tracks the measured data in the experiment with good performance. However, when the terminal voltage is close to the lower limit, the estimated anode potential increases rapidly. This causes an increase of estimation error in the anode potential with low +estimation error. At the same time, the cathode potential tracks its real value well and has less estimation error in the whole operating region. To compare the result numerically, the RMSE value of the estimated cathode and anode potential of the whole region is 0.0259 V and 0.0375 V, respectively.

The former case uses a drive cycle from NEDC, which has a lower continous current discharge rate. In order to further verify the effectiveness of the designed observer, another case uses the load profile of Motorway driving cycle, which is obtained from a prototype vehicle road test, to test the performance of the observer. This profile has a higher discharge rate and is closer to the actual application of electric vehicle. In the test, the battery has the 100% initial SOC before connecting to the load current, and the current is cut-off when the terminal voltage reduced to 2.5 V. The whole process takes about 58 min, and the result is shown in Fig. 17. The comparison between the estimated cathode and anode potentials by the observer and their actual values is shown Fig. 17(c) and (d). The results show that at higher current rates, the observer still can track the actual cathode and anode potentials with an average estimation error of less than 0.1 V.

5.4. Observer test with initial error of SOC

In the previous two tests, the initial condition of observer is set the

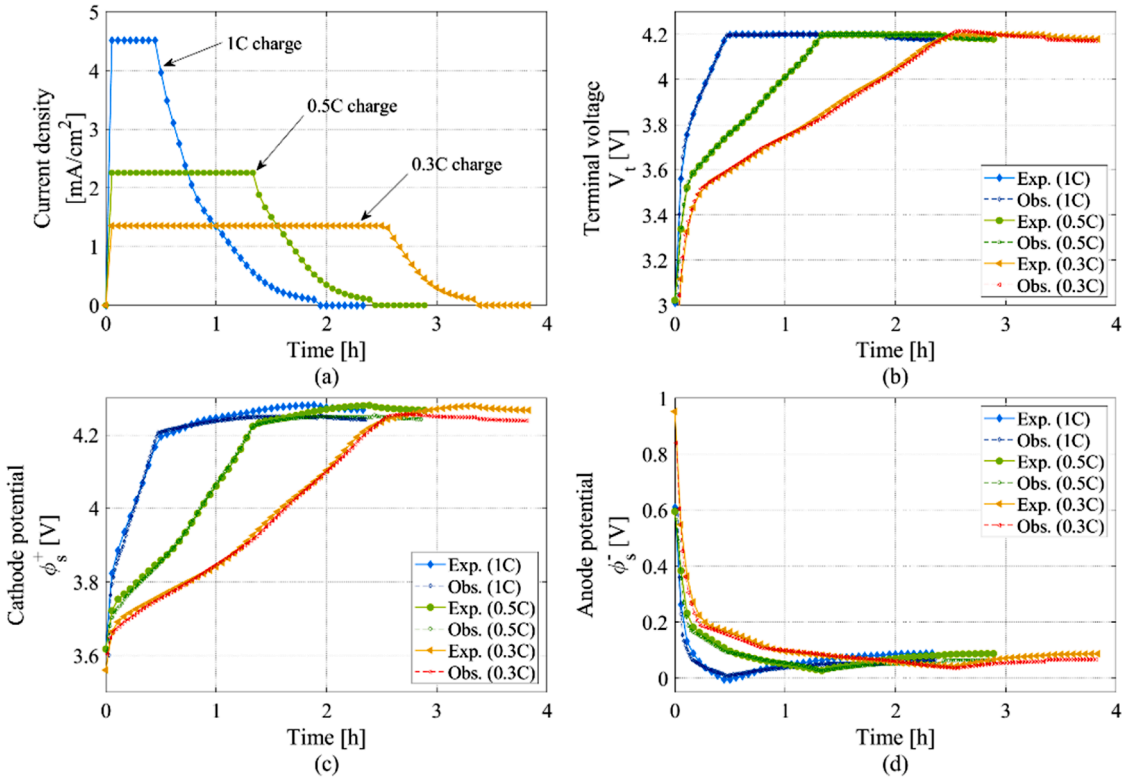

Fig. 13. Observer estimation of cathode and anode potentials to experimental battery reference during CC—CV charge with 0.3, 0.5 and 1C rate. a) Applied charging current; b) Terminal voltage; c) Cathode potential; d) Anode potential.

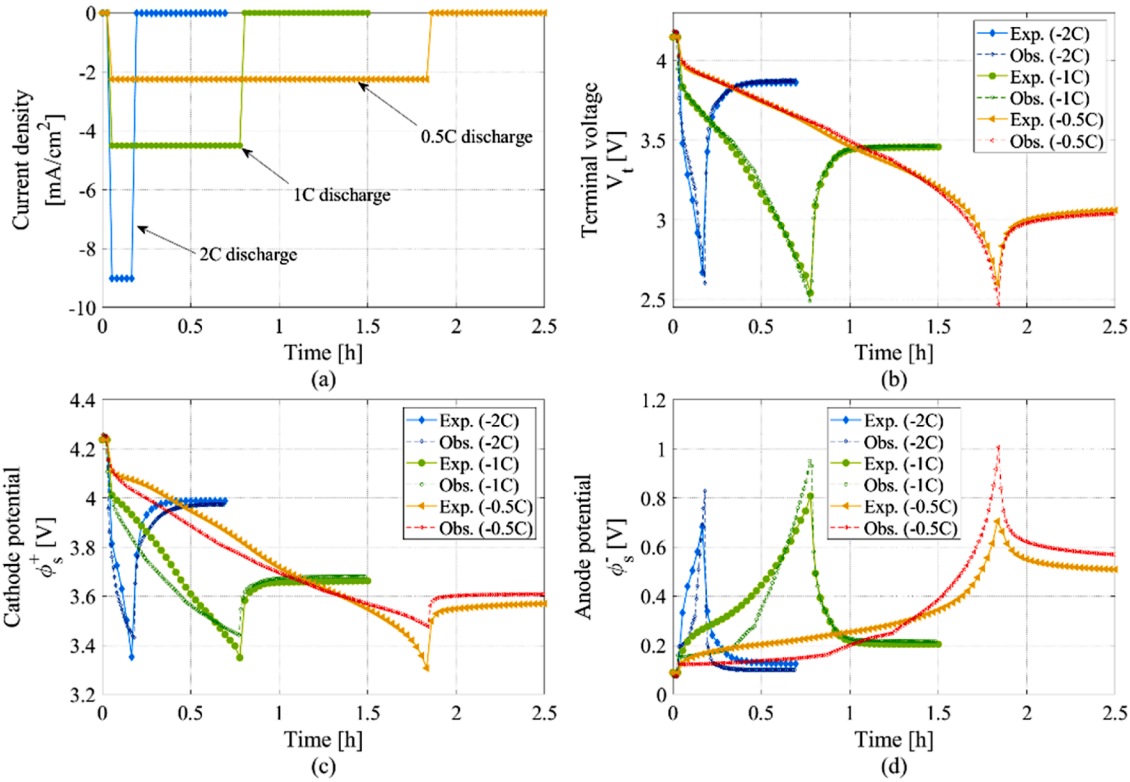

Fig. 14. Observer estimation of cathode and anode potentials to experimental battery reference during CC discharge with 0.5, 1 and 2C rate. a) Applied discharging current; b) Terminal voltage; c) Cathode potential; d) Anode potential.

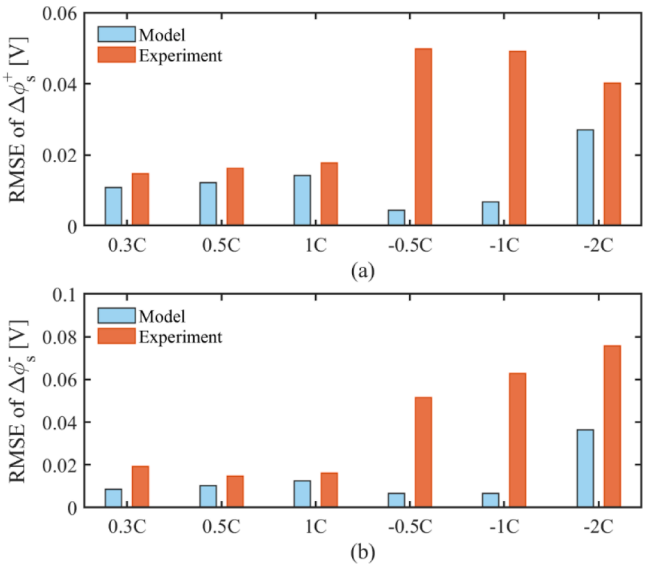

Fig. 15. Model validation of comparing experiment, FOM, ROM and LM on cathode and anode potential during CC discharge.

same with that in the experiment test that the PAT-cell is fully charged. However, in practice, it is difficult to ensure that the initial condition is known accurately. Therefore, the observer should be able to manage the initial error of SOC and compensate during operation. The next test aims to test the robustness of the observer under initial error of SOC.

In the next case study, the PAT-cell is not fully charged and operates using the same real-world drive cycle for discharge. But the observer is set with the initial condition of 100% SOC. The test result is shown in Fig. 18. In the result, the observer estimated terminal voltage starts from 4.2 V while the real terminal voltage of PAT-cell is only 3.6 V. The estimated cathode potential and anode potential both have initial estimation error. With the feedback of terminal voltage error, the observer starts to track the real value of the terminal voltage.

The comparison of estimated terminal voltage, cathode potential and anode potential between measured value in experiment and estimated value from observer are shown in Fig. 18(a) to (c), and their absolute estimation error are given in Fig. 18(d) to (f). From the result, it can be found that the initial estimation error of cathode potential is approximately 0.5 V and the estimation error of the anode potential is about 0.12 V. During the observer operation, the estimation error is reduced. From the results shown, the observer output converges to eliminate 90% initial error within 30 s. After about 120 s, the estimation error caused by the initial error of SOC can be fully eliminated in both cathode and anode potential estimation. The average estimation error of cathode potential is around 0.01 V while that of anode potential is 0.02 V. This test result verifies that the observer is robust to the initial error of SOC and able to eliminate the uncertainty of SOC after a period of operation. This result shows that, whatever the initial SOC of a real cell, the observer is able to eliminate the initial error of SOC and be used in practice to estimate the cathode and anode potential.

6. Limitation and future work

Although this paper proposes a feasible solution to design an observer for real-time estimation of anode potential, this method has some limitations that need to be further explored. First, the model order reduction uses the RG approach. The RG method accelerates the calculation of the ODE-form solution and performs well in a wide frequency range. However, it is sensitive to initial estimations and does not guarantee global optimality and convergence. In addition, the parametrisation is based on experimental tests at a constant temperature. If the battery has significant parameter variations due to temperature

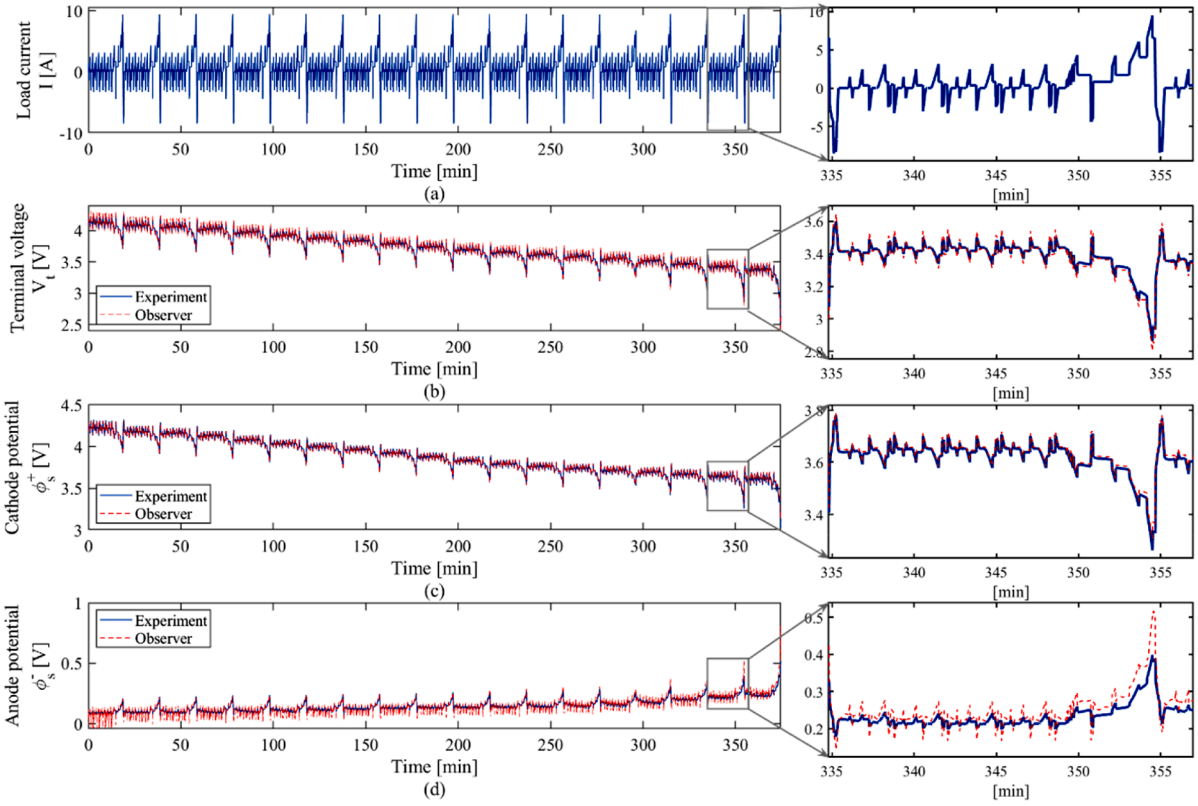

Fig. 16. Observer estimation to experimental PAT-cell with NEDC drive cycle of electric vehicles. a) Applied load current; b) Terminal voltage; c) Cathode potential; d) Anode potential.

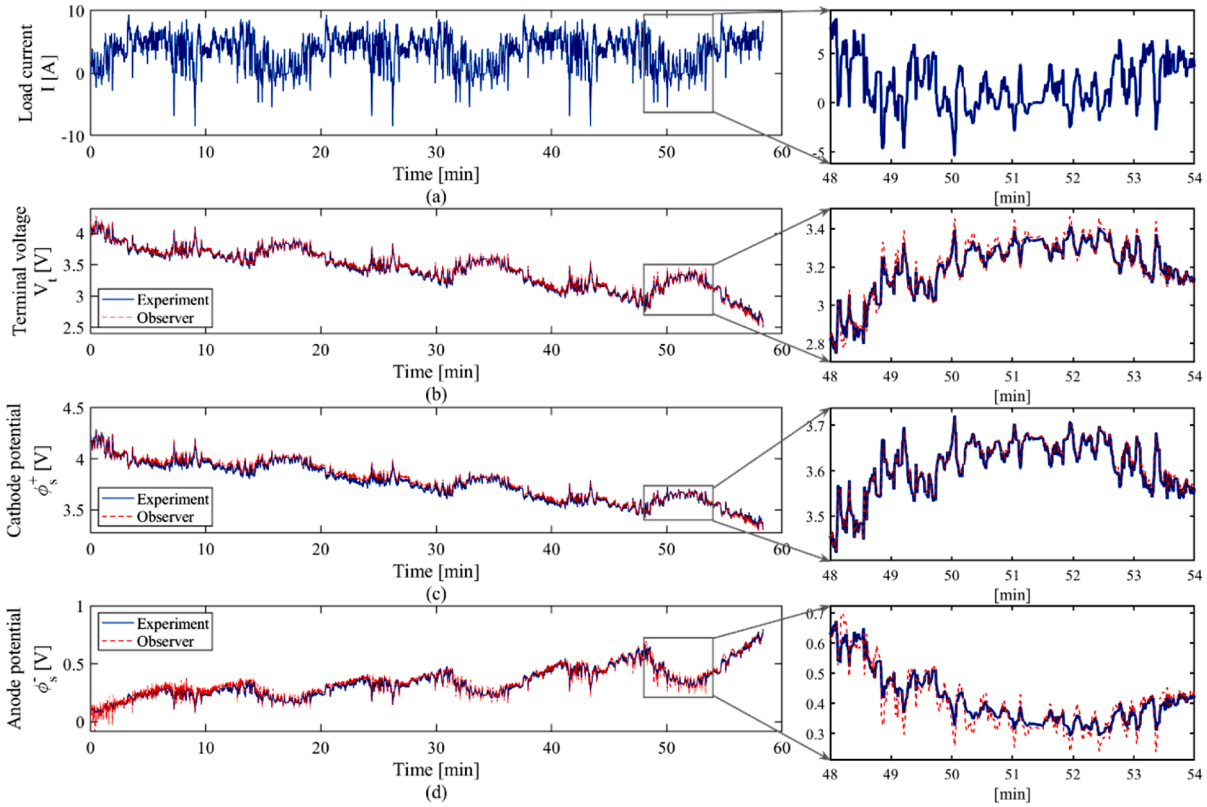

Fig. 17. Observer estimation to experimental PAT-cell with Motorway drive cycle of electric vehicles. a) Applied load current; b) Terminal voltage; c) Cathode potential; d) Anode potential.

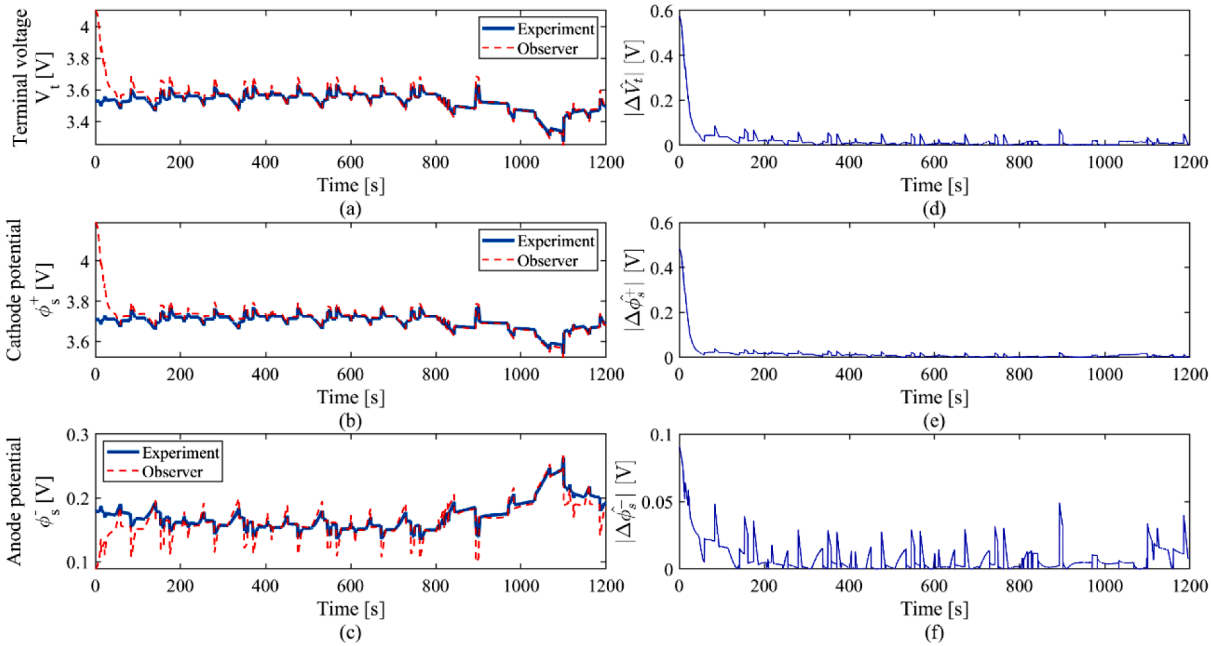

Fig. 18. Observer estimation to experimental PAT-cell with initial error of SOC. a) Terminal voltage; b) Cathode potential; c) Anode potential; d) Absolute estimation error of terminal voltage; e) Absolute estimation error of cathode potential; f) Absolute estimation error of anode potential.

changes or degradation, the observer estimation result could be far from the actual value. Therefore, these limitations will become our next work goals to be resolved in our future work.

In future studies, we will do the following work.

- Develop the SPMe model with thermal behaviour in order to consider the temperature effects to the cell in the electrochemical model and update the observer for estimating its thermal behaviour in real time.
- Validate the model and observer using a commercial cell of LGM50 21700 rather than a three electrodes PAT-cell and the transferability

of the model/observer to other cell formats and chemistries will be in investigated.
- Look more closely at the subject of fast charging with higher C rate using the designed observer and embedded within a charging control system and power electronic charging hardware.

7. Conclusion

In order to prevent lithium plating and prolong the battery life, it is crucial for the advanced battery management system to monitor the anode electrode potential at different conditions. This paper proposes an observer for cathode and anode potential estimation based on an electrochemical model, the single particle model with electrolyte (SPMe). The observer linearises the reduced order SPMe model and uses the most commonly measured signals, the applied current and terminal voltage, for the cathode and anode potential estimation. The reduced-order SPMe model reduces the complexity of finite differential method based full-order model while the linearised model linearises the nonlinear dynamics of the reduced order SPMe model. The result validates that the linearised model reduces the complexity and computational cost by more than 99% simulation time of the full-order model. The observer performance is validated in the constant current constant voltage (CC—CV) charging and constant current (CC) discharging as well as the real-world drive cycle from electric vehicles. The observer estimation root mean square error (RMSE) of cathode potential and anode potential is less than 0.02 V in charging and less than 0.08 V in discharging. The higher charging/discharging current can reduce the observer performance, and this is one of the known limitations of the SPMe model. In future works, the further validation will be done at full cell level and verify the transferability of the observer approach to different cell formats and chemistries. In addition, the model and observer will be developed to predict the battery degradation or ageing. Furthermore, the observer will be embedded into a control system to support the development of battery management system.

Funding statements

This work is supported by the Faraday Institution Multi-Scale Modelling project [EP/S003053/1 grant number FIRG003].

CRediT authorship contribution statement

Liuying Li: Methodology, Software, Validation, Investigation, Writing – original draft. **Yaxing Ren:** Methodology, Software, Validation, Investigation, Writing – original draft. **Kieran O'Regan:** Resources, Validation. **Upender Rao Koleti:** Writing – original draft. **Emma Kendrick:** Resources, Validation. **W. Dhammika Widanage:** Conceptualization, Methodology, Supervision, Writing – review & editing. **James Marco:** Conceptualization, Methodology, Supervision, Writing – review & editing.

Declaration of Competing Interest

The authors declare that they have no known competing financial interests or personal relationships that could have appeared to influence the work reported in this paper.

References

[1] L. Zhang, et al., Hybrid electrochemical energy storage systems: an overview for smart grid and electrified vehicle applications, Renew. Sustain. Energy Rev. (2020), 110581.
[2] D. Anseán, et al., Fast charging technique for high power lithium iron phosphate batteries: a cycle life analysis, J. Power Source. 239 (2013) 9–15.
[3] Z. Guo, et al., Optimal charging method for lithium ion batteries using a universal voltage protocol accommodating aging, J. Power Source. 274 (2015) 957–964.
[4] D. Anseán, et al., Operando lithium plating quantification and early detection of a commercial LiFePO4 cell cycled under dynamic driving schedule, J. Power Source. 356 (2017) 36–46.
[5] S. Schindler, et al., Voltage relaxation and impedance spectroscopy as in-operando methods for the detection of lithium plating on graphitic anodes in commercial lithium-ion cells, J. Power Source. 304 (2016) 170–180.
[6] T. Waldmann, M. Kasper, M. Wohlfahrt-Mehrens, Optimization of charging strategy by prevention of lithium deposition on anodes in high-energy lithium-ion batteries–electrochemical experiments, Electrochim. Acta 178 (2015) 525–532.
[7] C.-.H. Chen, et al., Development of experimental techniques for parameterization of multi-scale lithium-ion battery models, J. Electrochem. Soc. 167 (8) (2020), 080534.
[8] S.P. Rangarajan, Y. Barsukov, P.P. Mukherjee, Anode potential controlled charging prevents lithium plating, J. Mater. Chem. A 8 (26) (2020) 13077–13085.
[9] Y. Li, et al., Errors in the reference electrode measurements in real lithium-ion batteries, J. Power Source. 481 (2021), 228933.
[10] W. Mei, et al., Experimental and numerical methods to investigate the overcharge caused lithium plating for lithium ion battery, Energy Storage Mater. 32 (2020) 91–104.
[11] U.R. Koleti, et al., The development of optimal charging strategies for lithium-ion batteries to prevent the onset of lithium plating at low ambient temperatures, J. Energy Storage 24 (2019), 100798.
[12] E. McTurk, et al., Thermo-electrochemical instrumentation of cylindrical Li-ion cells, J. Power Source. 379 (2018) 309–316.
[13] A. Seaman, T.-.S. Dao, J. McPhee, A survey of mathematics-based equivalent-circuit and electrochemical battery models for hybrid and electric vehicle simulation, J. Power Source. 256 (2014) 410–423.
[14] A. Tomaszewska, et al., Lithium-ion battery fast charging: a review, ETransportation 1 (2019), 100011.
[15] Q. Wang, et al., A novel consistency evaluation method for series-connected battery systems based on real-world operation data, IEEE Trans. Transport, Electrif. 7 (2) (2020) 437–451.
[16] L. Zhang, et al., Battery heating for lithium-ion batteries based on multi-stage alternative currents, J. Energy Storage 32 (2020), 101885.
[17] Q.-.K. Wang, et al., A unified modeling framework for lithium-ion batteries: an artificial neural network based thermal coupled equivalent circuit model approach, Energy 138 (2017) 118–132.
[18] U.R. Koleti, T.Q. Dinh, J. Marco, A new on-line method for lithium plating detection in lithium-ion batteries, J. Power Source. 451 (2020), 227798.
[19] U.R. Koleti, et al., The development of optimal charging protocols for lithium-ion batteries to reduce lithium plating, J. Energy Storage 39 (2021), 102573.
[20] X. Zhang, et al., A novel method for identification of lithium-ion battery equivalent circuit model parameters considering electrochemical properties, J. Power Source. 345 (2017) 21–29.
[21] X. Lin, Real-time prediction of anode potential in Li-ion batteries using long short-term neural networks for lithium plating prevention, J. Electrochem. Soc. 166 (10) (2019) A1893.
[22] P. Arora, M. Doyle, R.E. White, Mathematical modeling of the lithium deposition overcharge reaction in lithium-ion batteries using carbon-based negative electrodes, J. Electrochem. Soc. 146 (10) (1999) 3543.
[23] Y. Li, et al., Constrained ensemble Kalman filter for distributed electrochemical state estimation of lithium-ion batteries, IEEE Trans. Ind. Inform. 17 (1) (2020) 240–250.
[24] Y. Li, et al., Electrochemical model-based fast charging: physical constraint-triggered PI control, IEEE Trans. Energy Convers. (2021).
[25] P.C. Urisanga, et al., Efficient conservative reformulation schemes for lithium intercalation, J. Electrochem. Soc. 162 (6) (2015) A852.
[26] B. Suthar, et al., Optimal charging profiles with minimal intercalation-induced stresses for lithium-ion batteries using reformulated pseudo 2-dimensional models, J. Electrochem. Soc. 161 (11) (2014) F3144–F3155.
[27] V. Ramadesigan, et al., Efficient reformulation of solid-phase diffusion in physics-based lithium-ion battery models, J. Electrochem. Soc. 157 (7) (2010) A854.
[28] P.W.C. Northrop, et al., Efficient simulation and model reformulation of two-dimensional electrochemical thermal behavior of lithium-ion batteries, J. Electrochem. Soc. 162 (6) (2015) A940–A951.
[29] Z. Chu, et al., Non-destructive fast charging algorithm of lithium-ion batteries based on the control-oriented electrochemical model, Appl. Energy 204 (2017) 1240–1250.
[30] J.C. Hamar, et al., Anode potential estimation in lithium-ion batteries using data-driven models for online applications, J. Electrochem. Soc. 168 (3) (2021), 030535.
[31] F.B. Planella, M. Sheikh, W.D. Widanage, Systematic derivation and validation of a reduced thermal-electrochemical model for lithium-ion batteries using asymptotic methods, Electrochim. Acta (2021), 138524.
[32] V. Ramadesigan, et al., Efficient reformulation of solid-phase diffusion in physics-based lithium-ion battery models, J. Electrochem. Soc. 157 (7) (2010) A854.
[33] S. Dey, B. Ayalew, P. Pisu, Nonlinear robust observers for state-of-charge estimation of lithium-ion cells based on a reduced electrochemical model, IEEE Trans. Control Syst. Technol. 23 (5) (2015) 1935–1942.
[34] X. Hu, et al., A linear time-invariant model for solid-phase diffusion in physics-based lithium ion cell models, J. Power Source. 214 (2012) 40–50.
[35] Y. Zeng, et al., Efficient conservative numerical schemes for 1d nonlinear spherical diffusion equations with applications in battery modeling, J. Electrochem. Soc. 160 (9) (2013) A1565.
[36] Y. Li, et al., A physics-based distributed-parameter equivalent circuit model for lithium-ion batteries, Electrochim. Acta 299 (2019) 451–469.

[37] Y. Li, et al., Adaptive ensemble-based electrochemical-thermal-degradation state estimation of lithium-ion batteries, IEEE Trans. Ind. Electron. (2021).
[38] S.J. Moura, et al., Battery state estimation for a single particle model with electrolyte dynamics, IEEE Trans. Control Syst. Technol. 25 (2) (2016) 453–468.
[39] A.M. Bizeray, et al., Identifiability and parameter estimation of the single particle lithium-ion battery model, IEEE Trans. Control Syst. Technol. 27 (5) (2018) 1862–1877.
[40] S.G. Marquis, et al., An asymptotic derivation of a single particle model with electrolyte, J. Electrochem. Soc. 166 (15) (2019) A3693.
[41] G. Richardson, et al., Generalised single particle models for high-rate operation of graded lithium-ion electrodes: systematic derivation and validation, Electrochim. Acta 339 (2020), 135862.
[42] M.G. Hennessy, I.R. Moyles, Asymptotic reduction and homogenization of a thermo-electrochemical model for a lithium-ion battery, Appl. Math. Model. 80 (2020) 724–754.
[43] A. Jokar, et al., Review of simplified Pseudo-two-Dimensional models of lithium-ion batteries, J. Power Source. 327 (2016) 44–55.
[44] J.N. Reddy, D.K. Gartling, The Finite Element Method in Heat Transfer and Fluid Dynamics, CRC press, 2010.
[45] S. Pramanik, S. Anwar, Electrochemical model based charge optimization for lithium-ion batteries, J. Power Source. 313 (2016) 164–177.
[46] S.G. Marquis, et al., A suite of reduced-order models of a single-layer lithium-ion pouch cell, J. Electrochem. Soc. 167 (14) (2020), 140513.
[47] I.R. Moyles, et al., Asymptotic reduction of a porous electrode model for lithium-ion batteries, SIAM J. Appl. Math. 79 (4) (2019) 1528–1549.
[48] K.A. Smith, C.D. Rahn, C.-.Y. Wang, Model order reduction of 1D diffusion systems via residue grouping, J. Dyn. Syst. Meas. Control 130 (1) (2008).
[49] M. Jun, K. Smith, P. Graf, State-space representation of Li-ion battery porous electrode impedance model with balanced model reduction, J. Power Source. 273 (2015) 1226–1236.
[50] K.E. Thomas, J. Newman, R.M. Darling, Mathematical Modeling of Lithium batteries, in Advances in Lithium-Ion Batteries, Springer, 2002, pp. 345–392.
[51] J.C. Forman, et al., Reduction of an electrochemistry-based li-ion battery model via quasi-linearization and pade approximation, J. Electrochem. Soc. 158 (2) (2010) A93.
[52] F.A. Ortiz-Ricardez, A. Romero-Becerril, L. Alvarez-Icaza, Residue grouping order reduction method in solid-phase lithium-ion battery models, J. Appl. Electrochem. (2021) 1–15.
[53] L. Li, et al., Control-oriented implementation and model order reduction of a lithium-ion battery electrochemical model, in: 2019 IEEE Vehicle Power and Propulsion Conference (VPPC), IEEE, 2019.
[54] K.A. Smith, C.D. Rahn, C.-.Y. Wang, Control oriented 1D electrochemical model of lithium ion battery, Energy Convers. Manag. 48 (9) (2007) 2565–2578.
[55] C. Fan, et al., Frequency domain non-linear characterization and analysis of lithium-ion battery electrodes, J. Energy Storage 36 (2021), 102371.
[56] M. Farag, M. Fleckenstein, S. Habibi, Continuous piecewise-linear, reduced-order electrochemical model for lithium-ion batteries in real-time applications, J. Power Source. 342 (2017) 351–362.
[57] R. Masoudi, J. McPhee, Application of Karhunen–Loéve decomposition and piecewise linearization to a physics-based battery model, Electrochim. Acta 365 (2021), 137093.
[58] T.G. Tranter, et al., Communication—prediction of thermal issues for larger format 4680 cylindrical cells and their mitigation with enhanced current collection, J. Electrochem. Soc. (2020).
[59] G. Dos Reis, et al., Lithium-ion battery data and where to find it, Energy and AI (2021), 100081.
[60] Y. Zhang, et al., A comparative study of Luenberger observer, sliding mode observer and extended Kalman filter for sensorless vector control of induction motor drives, in: 2009 IEEE Energy Conversion Congress and Exposition, IEEE, 2009.
[61] X. Duan, et al., Experimental study on the energy flow of a gasoline-powered vehicle under the NEDC of cold starting, Appl. Therm. Eng. 115 (2017) 1173–1186.
[62] G. Zhu, et al., Experimental study on combustion and emission characteristics of turbocharged gasoline direct injection (GDI) engine under cold start new European driving cycle (NEDC), Fuel 215 (2018) 272–284.